EFFECT OF STABILIZING ELEMENTS ON THE PRECIPITATION BEHAVIOR AND PHASE STABILITY OF TYPE 409 FERRITIC STAINLESS STEELS

by

Robert G. Nooning, Jr.

B.S., University of Pittsburgh, 1999

Submitted to the Graduate Faculty of

the School of Engineering in partial fulfillment

of the requirements for the degree of

Masters of Science in Materials Science and Engineering

University of Pittsburgh

2002

UNIVERSITY OF PITTSBURGH

SCHOOL OF ENGINEERING

This thesis was presented

by

Robert G. Nooning, Jr.

It was defended on

December 16, 2002

and approved by

Dr. J.C. Yang, Assistant Professor, Materials Science and Engineering

Dr. C.I. Garcia, Research Professor, Materials Science and Engineering

Thesis Advisor: Dr. A.J. DeArdo, William Keplar Whiteford Professor, Department of Materials Science and Engineering

ABSTRACT

EFFECT OF STABILIZING ELEMENTS ON THE PRECIPITATION BEHAVIOR AND PHASE STABILITY OF TYPE 409 FERRITIC STAINLESS STEELS

Robert G. Nooning, Jr., M.Sc.

University of Pittsburgh, 2002

Type 409 ferritic stainless steels have gained widespread use in the automotive industry in exhaust systems. Largely responsible for the acceptance of these steels is the stabilization with titanium and/or niobium which prevents sensitization due to the formation of chromium carbides. While both forms of stabilization (titanium or titanium plus niobium) have been demonstrated to be effective at preventing sensitization, the role of these alloying elements in the precipitation behavior and the formation of austenite has not been studied. It is therefore the aim of this research to study the precipitation behavior and the formation of austenite in these steels in the temperature ranges typical of hot rolling and annealing.

Two steels were studied in this research, a single stabilized titanium only Type 409, and a dual stabilized titanium plus niobium Type 409. First, thermodynamic models were used to predict the temperatures where carbides are expected to be stable in the two steels. Next, the initial as-received transfer bars of the two steels were characterized. A detailed analysis of the precipitates was conducted to characterize the size, composition, structure, and orientation relationship of the carbides. Subsequently, the steels were reheated in order to observe both the dissolution of the carbides and the formation of austenite in the temperature range of 700 to 1300 °C. The austenite formation was studied using EBSD in the SEM to characterize the grain

boundaries between the ferrite grains, and also to characterize the interfaces between the ferrite and the martensite (quenched austenite). Finally, continuous cooling deformation testing was used to determine the precipitation start temperatures of the steels and to study the formation of austenite during continuous cooling.

The main findings of this research were that the (Ti,Nb)C precipitates in the dual stabilized steel were stable to much higher temperatures than the TiC precipitates in the single stabilized steel. During continuous cooling, the dual stabilized steel precipitated carbides at 1210 °C, while the single stabilized steel did not precipitate carbides until 840 °C. These results are discussed and their possible effect on the final microstructure and mechanical properties are inferred.

ACKNOWLEDGEMENTS

I would like to express my appreciation and gratitude to my advisors Dr. A.J. DeArdo and Dr. C.I. Garcia for giving me the opportunity to complete this work and for all of their guidance along the way.

I would also like to thank Dr. M.J. Hua for all of his help in the TEM and atom probe. In addition to being an expert in both TEM and atom probe, Dr. Hua has always been available for help whenever needed, and for that I am very grateful.

Special thanks go to Dr. Goldman for his advice, and for taking the time to review any paper or thesis, without hesitation, in a very timely manner. Without his help, the process of writing a thesis or paper would be a much more difficult task.

Gratitude is expressed to all of the graduate students of BAMPRI who have always been there for me, and who were always there to help pass the long hours of a graduate student. A very special thanks goes to Mukul Renavikar, who has been the most valuable source of information that a graduate student could ever have, in addition to being one of the kindest people I will ever meet.

Finally, I would also like to thank my parents for all of their emotional and financial support whenever necessary. Although they are across the state, their support is with me always.

TABLE OF CONTENTS

LIST OF TABLES

Table Number **Page**

LIST OF FIGURES

Figure No. **Page**

1.0 INTRODUCTION

Over the past several decades ferritic stainless steels have seen a steady growth in production, due mostly to their use in automotive exhaust systems. Type 409, and ferritic stainless steels in general, exhibit many attractive qualities when compared to austenitic stainless steels. In terms of price, ferritic stainless steels have a lower cost due to their lower alloy content. Austenitic stainless steels require higher contents of austenite stabilizers such as nickel, manganese, and molybdenum that drive up the cost. Ferritic stainless steels exhibit good corrosion resistance under most conditions, but this requires keeping the chromium in solution. While austenitic stainless steels often contain 17-18 percent chromium or higher, type 409 ferritic stainless steel requires only the minimum 11 percent for corrosion resistance. This lower chromium content means that the steels must keep all of the chromium in solution or corrosion will occur. In an unstabilized state, these steels are susceptible to intergranular corrosion in the heat affected zone of weld joints. Researchers have found that small additions of titanium and/or niobium can stop the formation of chromium carbides and thus keep the chromium in solution. However, these additions can also affect the mechanical properties both as solutes and as precipitates. It is therefore very important to understand the dissolution and precipitation behavior of these steels. It is the objective of this thesis to determine the temperatures and times at which dissolution occurs and also characterize the precipitation in terms of time, temperature, composition and crystallography.

2.0 BACKGROUND

2.1 Classifications of Stainless Steels

Stainless steels are divided into five main classifications according to their microstructure; ferritic, austenitic, duplex, martensitic, and precipitation hardenable. Each of these types of stainless steels will be explained briefly in the following sections.

2.1.1 Ferritic Stainless Steels

Ferritic stainless derive their name from their BCC ferrite crystal structure, which is generally stable from room temperature up to the liquidus temperature. Ferritic stainless steels are the simplest type of stainless steels. Ferritic stainless steels contain approximately 11-30 percent chromium and only small amounts of other elements. Compositions of several ferritic stainless steel grades are given in Table 1. The chromium additions give the steel its corrosion resistance and also further stabilize the BCC crystal structure. Some of the drawbacks of ferritic stainless steels are their susceptibility to intergranular corrosion, the presence of a ductile-to-brittle transition temperature (DBTT), and lower stretch formability than their austenitic counterparts. Due to their adequate corrosion resistance and lower cost, ferritic stainless steels are chosen over austenitic steels in less severe applications as a replacement to mild carbon steels.

Table 1 Compositions of selected commercial grades of ferritic stainless steels

Alloy	C*	Cr	Ni	Mo	Other
Type 409	0.08	10.50/11.	-	-	Ti: 6 x C min
Type 430	0.12	16.0/18.0	-	-	-
Type 439	0.07	17.0/19.0	0.50	-	Ti: 12 x C min 0.15 Al max
Type 444	0.025	17.5/19.5	1.00	1.75/2.50	Ti + Nb: 0.2 + 4(C + N)
26-1	0.01	25.0/27.5	0.50	0.75/1.50	0.015N, 0.20Cu
26-3-3	0.025	25.0/27.0	1.50/3.5	2.50/3.50	Ti + Nb: 0.2 + 4(C + N)
29-4	0.010	28.0/30.0	0.15	3.50/4.20	0.15Cu, 0.02N
29-4C	0.03	28.0/30.0	1.00	3.60/4.20	Ti + Nb: 6(C + N)
29-4-2	0.01	28.0/30.0	2.00/2.5	3.50/4.20	0.15Cu, 0.02 N, 0.025(C + N)

2.1.2 Austenitic Stainless Steels

Austenitic stainless steels were one of the first types of stainless steels and today make up approximately 65 to 70 percent of the total U.S. stainless steel production. These steels contain 16 to 25 percent chromium and 7 to 10 percent nickel. Austenitic stainless steels have high nickel contents to stabilize the austenite at room temperature. They also contain higher chromium contents for increased corrosion resistance. Typical compositions of austenitic stainless steels are given in Table 2. The increased alloy contents create a higher cost product but the FCC austenite exhibits very high ductility resulting in a material with good formability and very good corrosion resistance.

2.1.3 Duplex Stainless Steels

Duplex stainless steels contain a mixture of ferrite and austenite at room temperature in an attempt to combine the beneficial properties of the two types of steels. These steels contain 18-30 percent chromium and an intermediate amount of nickel (3-9 percent) that is not enough for a fully austenitic structure at room temperature (compositions shown in Table 3). Duplex

stainless steels have intermediate levels of corrosion and mechanical properties. This includes a higher resistance to stress corrosion and higher strength than austenitic steels but lower resistance to stress corrosion and lower strength than ferritic stainless steels. The toughness is also lower than that of the austenitic stainless steels but higher than that of the ferritic stainless steels.

Table 2 Compositions of select grades of austenitic stainless steels

Alloy	C*	Mn*	Cr	Ni	Mo	Si*	Other
Cr-Ni Austenitic Grades							
Type 304 (S30400)	0.08	2.00	18.0/20.0	8.00/10.6	-	1.00	-
Type 304L (S30403)	0.03	2.00	18.0/20.0	8.00/12.0	-	1.00	-
Type 316 (S31600)	0.08	2.00	16.0/18.0	10.0/14.0	2.00/3.00	1.00	-
Type 316L(S31603)	0.03	2.00	16.0/18.0	10.0/14.0	2.00/3.00	1.00	-
Type 321 (S32100)	0.08	2.00	17.0/19.0	9.00/12.0	-	-	Ti: 5 x C
Cr-Mn Austenitic Grades							
Type 204L (S20403)	0.03	7.50/10.0	17.0/19.0	4.00/6.00	-	1.00	-
Type 216L (S21603)	0.03	7.50/9.00	17.5/22.0	5.00/7.00	2.00/3.00	1.00	-
22-13-5 (S20910)	0.06	4.00/6.00	20.5/23.5	11.5/13.5	1.50/3.00	1.00	-
18-18 Plus (S28200)	0.15	17.0/19.0	17.0/19.0	-	0.50/1.50	1.00	-

Table 3 Typical compositions of duplex stainless steels

Alloy	C	Mn	Cr	Ni	Mo	Si	Other
Type 329 (S32900)	0.08	1.00	23.0/28.0	2.50/5.00	1.00/2.00	0.75	-
2205 (S31803)	0.03	2.00	21.0/23.0	4.50/6.50	2.50/3.50	1.00	0.08/0.20 N
255 (S32550)	0.04	1.50	24.0/27.0	4.50/6.50	2.00/4.00	1.00	Cu 1.50-2.50

2.1.4 Martensitic Stainless Steels

Martensitic stainless steels contain 12-17 percent chromium for good corrosion resistance. However, since chromium is a strong ferrite stabilizer, a strong austenite stabilizer must be added so that austenite can form during annealing. As will be seen in Section 2.2.4, carbon is a very strong austenite stabilizer. Therefore, these steels have high carbon contents to

stabilize the austenite at high temperatures. The high carbon content will also increase the strength through solid solution strengthening and the precipitation of a large number of (Fe, Cr) carbides. The chromium, in addition to adding to the corrosion resistance, also greatly increases the hardenability of these steels, and along with the silicon and manganese allows for an air-cooled, fully hardened, microstructure. Typical compositions are given in Table 4. These steels are also tempered for increased ductility and toughness. In general, martensitic stainless steels have higher strength, but are offset by lower toughness, ductility, and corrosion resistance when compared to ferritic or austenitic stainless steels.

Table 4 Typical compositions of martensitic stainless steels

Alloy	C	Mn	Cr	Ni	Mo	Si	Other
Type 410 (S41000)	0.15	1.00	11.5/13.5	-	-	1.00	-
Type 420 (S42000)	>0.15	1.00	12.0/14.0	-	-	1.00	-
Type 440C (S44004)	0.95/1.20	1.00	16.0/18.0	-	0.75	1.00	-

2.1.5 Precipitation Hardenable Stainless Steels

Precipitation Hardenable steels are divided into two groups, semiaustenitic and martensitic. The semiaustenitic steels are austenitic but can be transformed to martensite by simple thermal and/or mechanical treatments. The martensitic group is composed of 100% martensite after a simple anneal and air cool treatment. Precipitation hardenable steels contain aluminum (which forms NiAl and Ni_3Al) and/or copper (which forms a highly dispersed copper phase) for precipitation hardening and require a heat treatment in the 480 to 650 °C range, much like precipitation hardening in aluminum alloys. Precipitation hardening steels can demonstrate good mechanical and chemical properties such as high strength, good ductility, and good corrosion resistance.

Table 5 Typical compositions of precipitation hardenable stainless steels

Alloy	C*	Mn*	Cr	Ni	Mo	Si	Other
17-4 PH (S17400)	0.07	1.00	15.5/17.5	3.00/5.00	0.75	1.00	3-5 Cu, 0.15-
17-7 PH (S17700)	0.09	1.00	16.0/18.0	6.50/7.75	-	1.00	0.45 Nb
15-7 Mo (S15700)	0.09	1.00	14.0/16.0	6.50/7.75	2.00/3.00	1.00	0.75-1.50 Al

2.2 Ferritic Stainless Steels

2.2.1 General Characteristics of Type 409 Ferritic Stainless Steel

There are several characteristics of ferritic stainless steels that are important to keep in mind during selection, processing, and service of the alloy. Type 409 is the most basic stainless steel, containing only 11 percent chromium and a stabilizing element. The eleven percent chromium gives type 409 only a minimum amount of corrosion protection and further stabilizes the BCC ferrite phase field. This crystal structure difference between ferritic and austenitic stainless steels gives the two very different mechanical properties. Room temperature yield strengths are typically comparable to those of austenitic alloys. However, the austenitic stainless steels have a higher work hardening rate which results in a higher ultimate tensile strength. The higher work hardening rate for austenitic stainless steels also results in better stretch formability compared to ferritic stainless steels. The ferritic stainless steels do have better deep drawability because of the strong {111} texture inherent to the BCC microstructure, which makes them well suited for automotive exhaust parts. Another characteristic of ferritic stainless steels that separates them is the presence of a ductile to brittle transition temperature (DBTT), which can cause brittle fracture prematurely. The use of ferritic stainless steels in many applications will depend on increasing the formability and decreasing the ductile to brittle transition temperature.

The formability of ferritic stainless steels can be improved in several ways. One method is to increase the amount of {111} texture component in the steel. Figure 1[1] shows the effect of {111} texture on the average plastic strain ratio, r-bar, and thus the deep drawability, of an AKDQ steel. The average plastic-strain ratio is defined as $(r_0 + 2r_{45} + r_{90}) / 4$, where r is the lankford parameter, as defined by Lankford et al[2]. in the 1950's. The lankford parameter is a measure of the normal anisotropy of sheet materials, as measured by the ratio of width strain to thickness strain. The {111} texture component is higher in ferritic steels than austenitic steels because of the BCC microstructure, but can be improved further through controlled hot rolling. Another way to increase the formability is to decrease the interstitial carbon and nitrogen contents. Lower carbon contents will increase the formability of steels by increasing the mean r-value (Figure 2[3]).

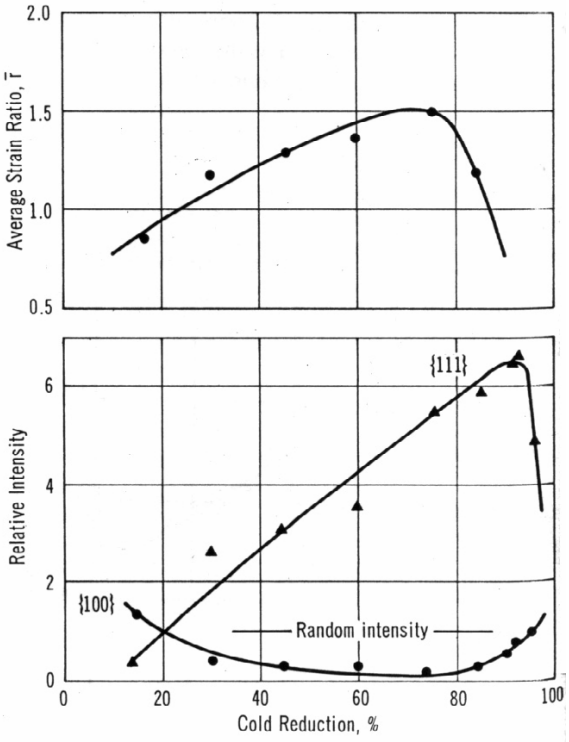

Figure 1 Effect of {111} texture component on r. As the relative intensity of {111} component increases the average strain ratio increases

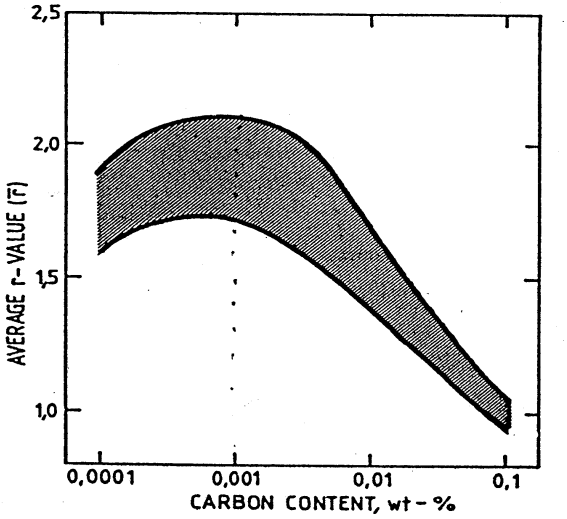

Figure 2 Effect of carbon on the average strain ratio

Reducing the carbon content has been shown to increase the weldability of ferrite-pearlite steels, as shown in the Graville Diagram (Figure 3[4]). Decreasing the carbon content has also been shown to decrease the ductile-to-brittle transition temperature (Figure 4). The DBTT can also be decreased by decreasing the grain size of the steel, which will also increase the strength, ductility, and formability.

There are also several embrittlement mechanisms present in ferritic stainless steels that must be taken into account during processing and service. Ferritic stainless steels can be susceptible to intergranular corrosion due to sensitization. Sensitization occurs when some of the chromium is taken out of solution through the formation of chromium carbides. Because these steels only have the minimum amount of chromium necessary for passivation (Section 2.2.5), this reduction in chromium at the grain boundaries leads to intergranular corrosion. For this reason, titanium and/or niobium are added to the steels to tie up all of the available carbon. Other important embrittlement mechanisms are 475 °C embrittlement and sigma phase embrittlement. These embrittlement mechanisms will be discussed further in Section 2.3.

2.2.2 Uses of Ferritic Stainless Steels

Ferritic stainless steels are mainly used in the automotive exhaust systems as a compromise between inexpensive low carbon steels and higher cost, higher alloyed ferritic or austenitic stainless steels. The ferritic alloys have better corrosion resistance and thus a longer life than low carbon steels and have a lower cost than the more highly alloyed stainless steels. The corrosion resistance of Al-plated carbon steel, type 409 stainless steel, and type 436 high Cr (17%Cr-1%Mo) ferritic stainless steel in an activated carbon synthetic condensate, is shown in Figure 5[5]. It is clear that as the price increases, the corrosion resistance increases. The stainless

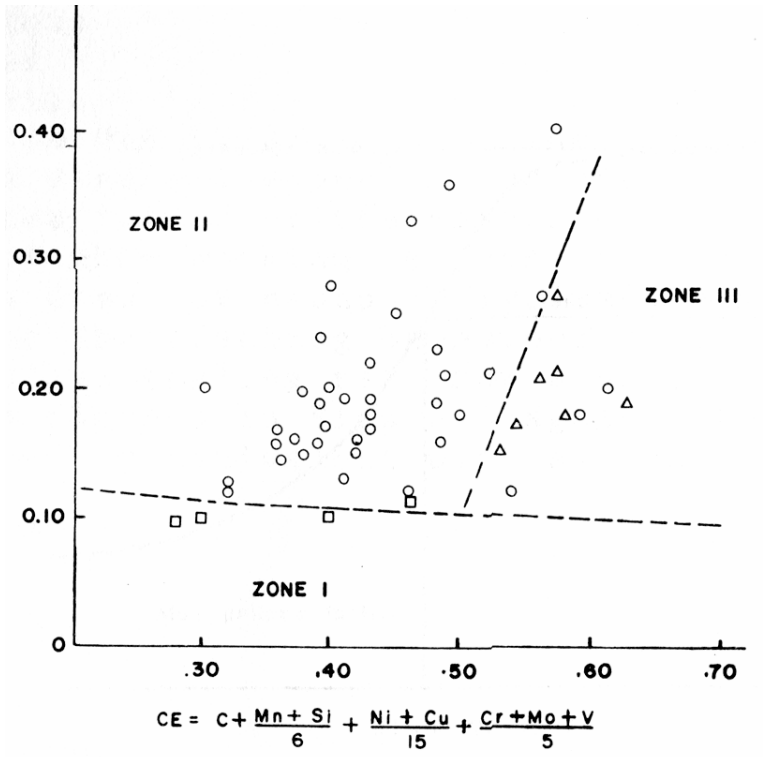

Figure 3 Graville welding diagram

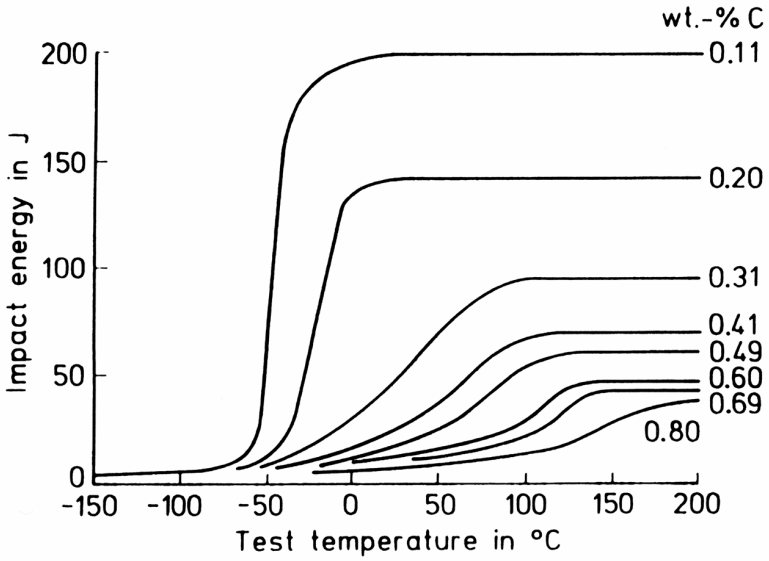

Figure 4 Effect of carbon on DBTT

steel exhaust system is composed of a hot and a cold end as shown in Figure 6[6]. As can be seen, most of the parts are made of various 11% Cr ferritic stainless steel grades, except for those parts in more demanding heat and corrosion areas. These parts are usually made of higher chromium ferritic alloys or austenitic stainless steels.

2.2.3 The Iron-Chromium System

The two main components of a ferritic stainless steel are iron and chromium. It is therefore important to consider the iron-chromium phase diagram shown in Figure 7. The iron-chromium system has a BCC solid solution through the entire composition and temperature range of the phase diagram below 1500 °C except for two notable areas. At high temperatures (830-1400 °C) and low chromium contents (<12.7%), there is an austenite phase loop and at intermediate chromium contents (~15-70%) and low temperatures (500-800 °C), there is a hard, brittle, tetragonal phase known as sigma phase. The sigma phase can be a source of embrittlement in these steels and will be discussed in Section 2.3. Because T409 ferritic stainless steels contain only eleven percent chromium, it is possible to form austenite during processing. Since eleven percent chromium is near the nose of the austenite loop, small fluctuations in chromium contents can dramatically change the phase balance between ferrite and austenite during hot rolling.

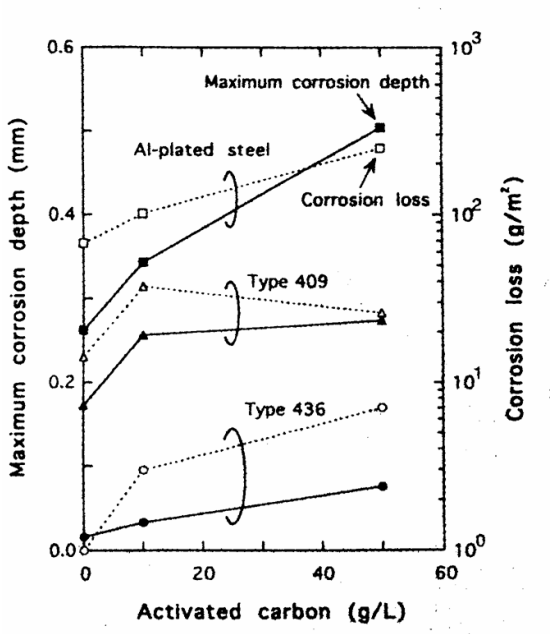

Figure 5 Corrosion rates of an Al-plated carbon steel, type 409 ferritic stainless steel, and type 436 high chromium stainless steel

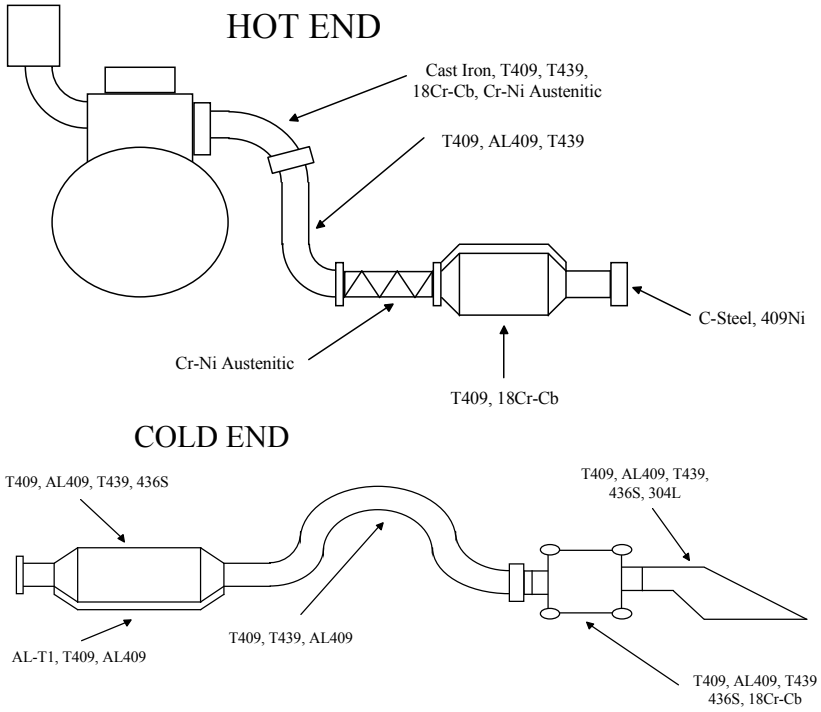

Figure 6 Types of steels used in a typical automotive exhaust system

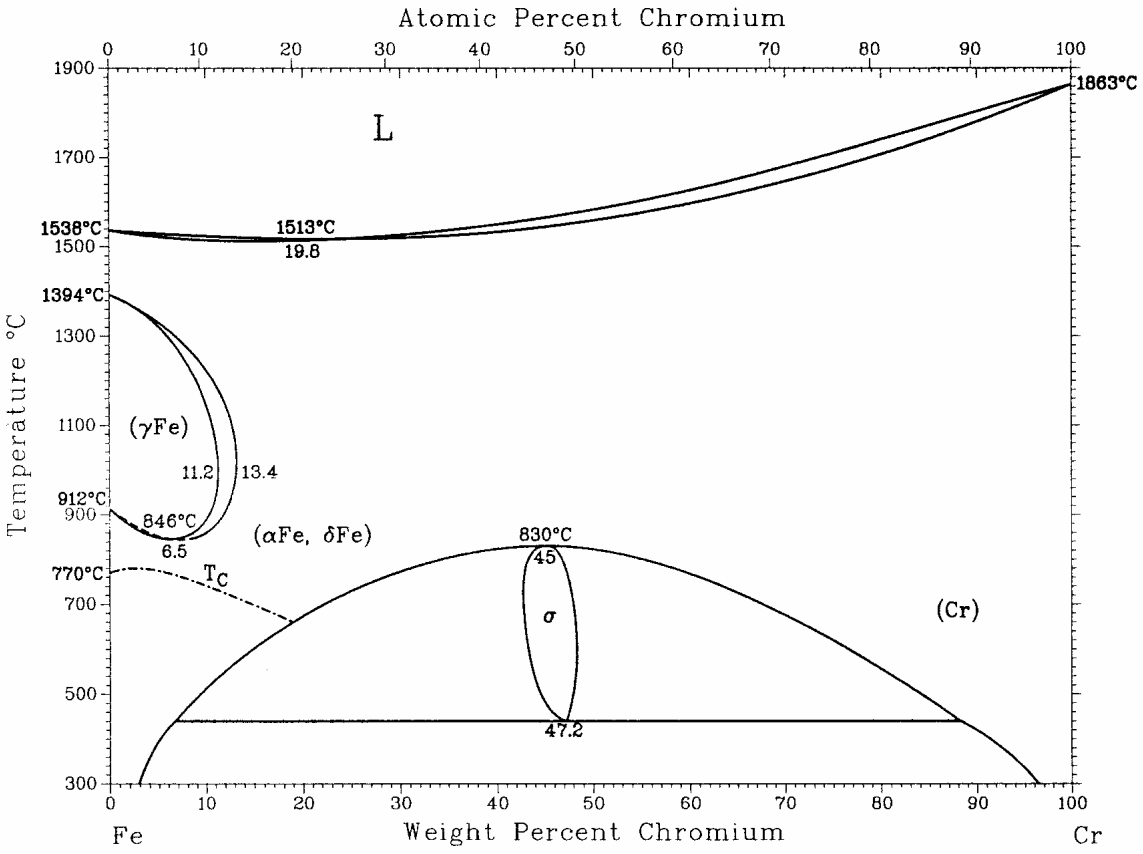

Figure 7 Iron-Chromium Phase Diagram

2.2.4 Effects of Interstitial Carbon and Nitrogen

While small changes in the temperature or chromium content will shift the phase balance during hot rolling and can cause variability, the situation can be compounded by the effects of carbon and nitrogen on the phase diagram. Carbon and nitrogen will shift the location of the austenite loop to higher temperatures and higher chromium contents as shown in Figure 8[7]. The result is that small fluctuations in carbon, nitrogen, or chromium can change the amount of austenite at high temperatures. This can be demonstrated by looking at an Fe-Cr-C pseudo-binary phase diagram. Figure 9 shows a pseudo-binary phase diagram generated by Thermo-Calc with Fe-12%Cr on one axis and carbon on the other axis. This diagram demonstrates how small changes in the carbon content can increase the size of the austenite and two phase fields.

2.2.5 Passivation

Stainless steels get their corrosion resistance from a thin chromium oxide layer that adheres to the surface. This layer then acts as a protective coating to stop further oxidation and this process is known as passivation[11,15].

2.3 Embrittlement Phenomena

There are three main embrittlement mechanisms in ferritic stainless steels. They are 475 °C embrittlement, sigma phase embrittlement, and high temperature embrittlement or sensitization. Of these three phenomena, sensitization presents the most problems because it can occur during normal fabrication processes. The other phenomena require long periods of time at elevated temperatures to occur and thus are not usually encountered during fabrication of the final part. All three mechanisms will be discussed in the following sections.

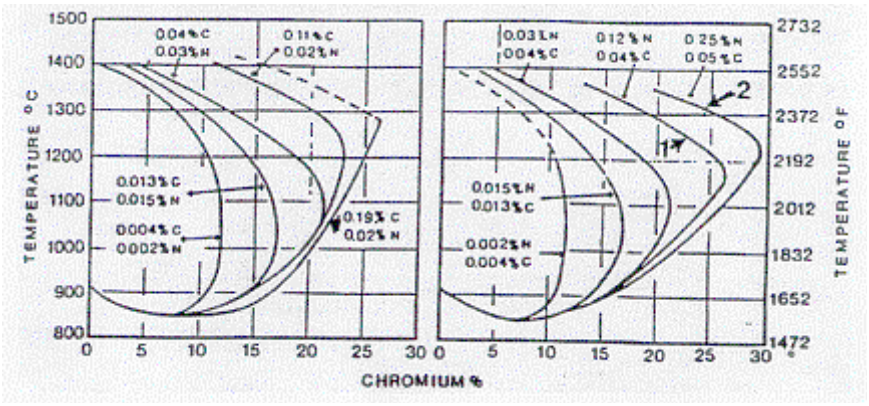

Figure 8 Effect of carbon and nitrogen on the austenite phase field

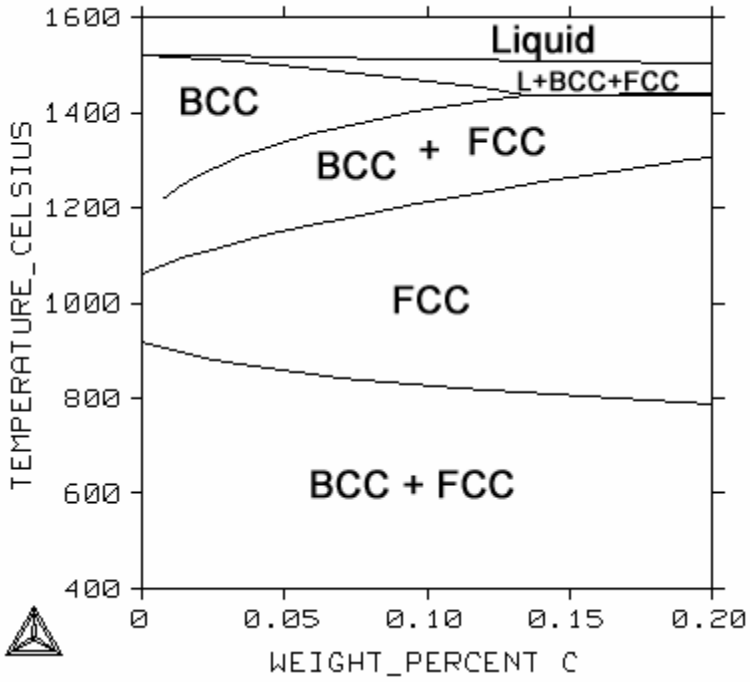

Figure 9 Fe-11%Cr –C pseudo-binary phase diagram generated by Thermocalc

2.3.1 High Temperature Embrittlement (Sensitization)

In polycrystalline materials, grain boundaries are often the catalyst for many reactions. This is because grain boundaries differ both physically and chemically from either one of the grains they separate. Grain boundaries typically have higher concentrations of vacancies, solutes, and impurities. Diffusion rates are also higher at grain boundaries. Using the destruction of part of a grain boundary to decrease the surface energy required for nucleation, precipitates can nucleate more easily at grain boundaries than in the matrix. Precipitates will also tend to nucleate at grain boundaries due to the segregation of solute and impurity atoms to the grain boundaries. In ferritic stainless steels, these elements are carbon and nitrogen. If there is free carbon and nitrogen at high temperatures, chromium carbides form along the grain boundaries. Because the diffusion of carbon is faster than the diffusion of chromium, the region near the grain boundary becomes depleted of chromium as the chromium carbide grows. This leaves the grain boundary concentrations of chromium below the 11 percent necessary for passivation which leads to intergranular corrosion. A schematic diagram showing the chromium carbides and the resulting chromium depleted zone, is shown in Figure 10. Precipitation of chromium carbonitrides requires a slow cool through the temperature range of 500-700°C. Above 700 °C, the diffusion of chromium is fast enough to replenish the chromium at the grain boundaries and below 500 °C, the diffusion of carbon is too slow for the precipitates to form. One place where this slow cool can occur is in the heat affected zone (HAZ) in the vicinity of a weld joint.

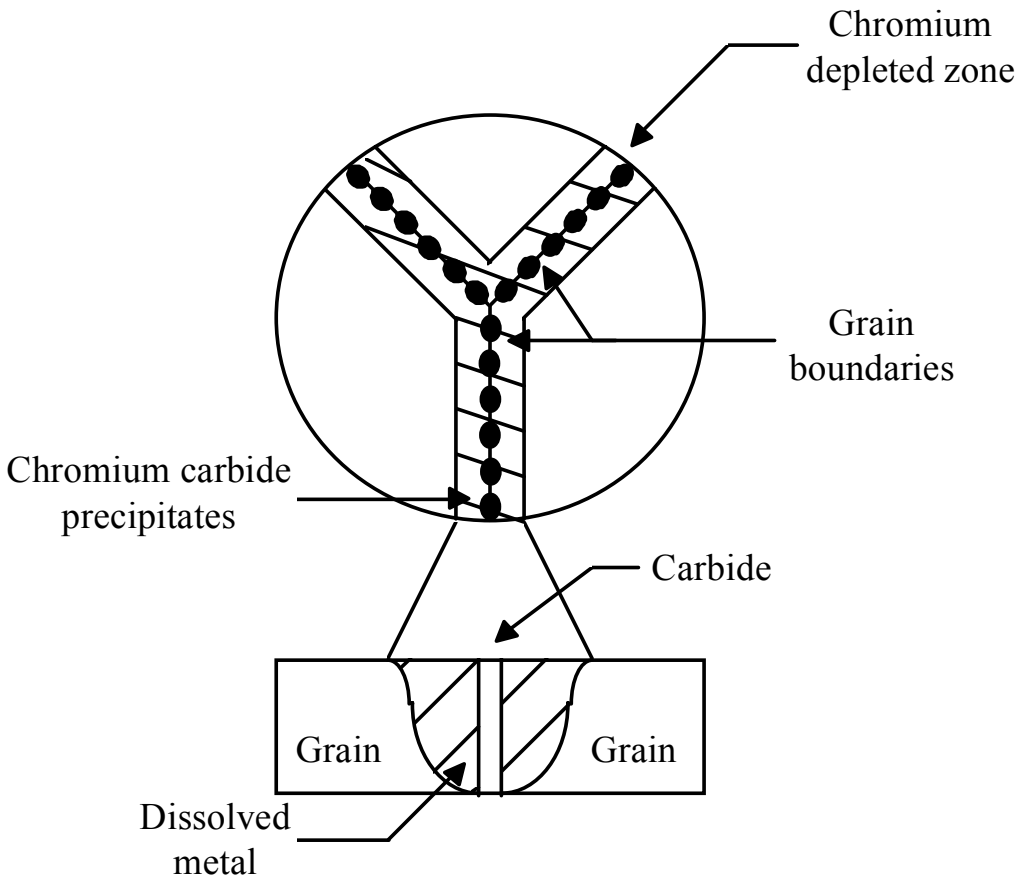

Figure 10 Schematic diagram of a grain boundary with chromium carbide precipitates showing a chromium-depleted zone near the grain boundary

Sensitization can be avoided by one of several methods, all of which increase the production cost of the steel:

1.) Re-solution heat treatment after welding. Reheating the steel to between 950 and 1100 °C and then cooling rapidly will dissolve the chromium carbides and avoid re-precipitation during cooling.
2.) Retard the kinetics of sensitization through molybdenum additions, which lengthen the time required for sensitization.
3.) Reduce interstitial levels by better control during steelmaking. Advances in steelmaking during the 1980's such as AOD and VOD technology have allowed the production of very low carbon levels.
4.) Carbon and Nitrogen levels can be further reduced by addition of strong carbide and nitride forming elements such as titanium, niobium, and zirconium. This is called stabilization and will be discussed in Section 2.4.

2.3.2 475 °C Embrittlement

This type of embrittlement occurs when ferritic stainless steels are heated for long times in the temperature range of 400-500 °C. When heated in this temperature range for long periods of time, an increase in strength and a large decrease in ductility is observed (Figure 11[8]). The embrittlement has been attributed to the precipitation of a chromium rich sigma phase on the dislocations. In steels with less than 18% chromium, the precipitation occurs by a nucleation and growth mechanism while the reaction proceeds by spinodal decomposition in higher chromium stainless steels[9]. Lower chromium contents will increase the incubation time and thus decrease

the likelihood of 475 °C embrittlement. Therefore, the kinetics in low Cr T409 are very slow and 475 °C embrittlement is not usually a concern.

2.4 Stabilization

To combat the problem of sensitization, the carbon in ferritic stainless steels is reduced through a combination of steelmaking practices and the addition of elements with a strong affinity for carbon and nitrogen. First, these steels are processed in an AOD or VOD to reduce the carbon content to very low levels (<0.02). The carbon and nitrogen in solution are then further reduced through the addition of titanium and/or niobium. Titanium and niobium form carbonitrides which precipitate at higher temperatures and shorter times than chromium carbides, thus removing all of the carbon from solution before the chromium carbides have a chance to form. This can be shown schematically by superimposing the kinetic CCP curves for chromium carbide precipitation and microalloy carbide precipitation (Figure 12). Either titanium or titanium plus niobium additions have been used, and the two methods will be compared in the following section.

2.4.1 Titanium-Only Stabilization

Titanium stabilized type 409 was first utilized in the automotive exhaust systems in 1961 for the Ford Thunderbird[10]. Initial stabilization requirements were 6 times the carbon concentration with a minimum of 0.75 percent[11]. These steels were probably not fully stabilized based on the O, N, and S levels available to the steelmaking technologies of the time[12]. Once AOD and VOD technologies were introduced in the 1980's, interstitial levels were reduced and the titanium additions were reduced as well. However, even the newer low interstitial ferritic

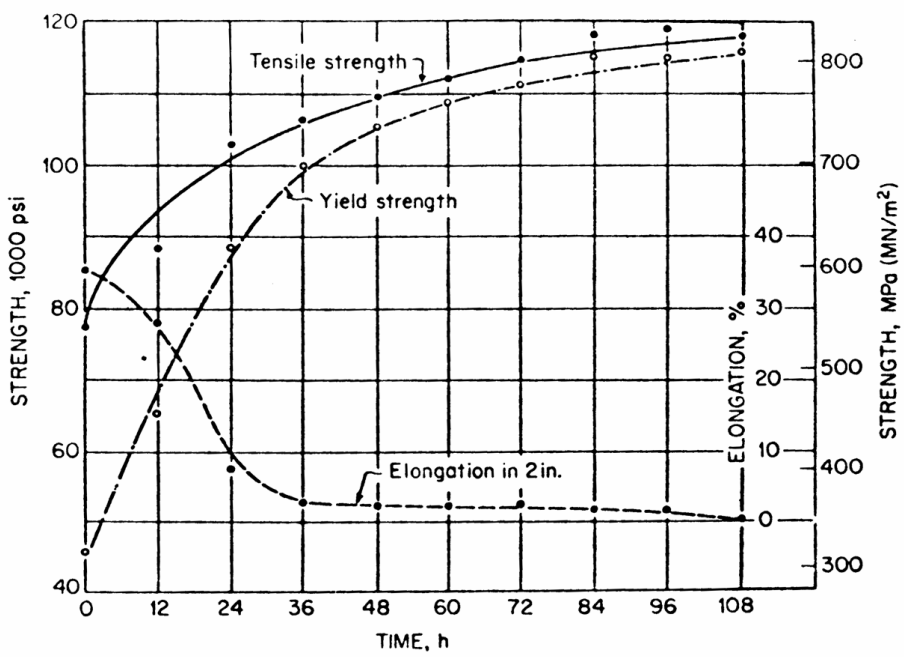

Figure 11 Plot of embrittlement at 475 °C. At longer times, precipitation of sigma phase causes an increase in strength and a decrease in ductility

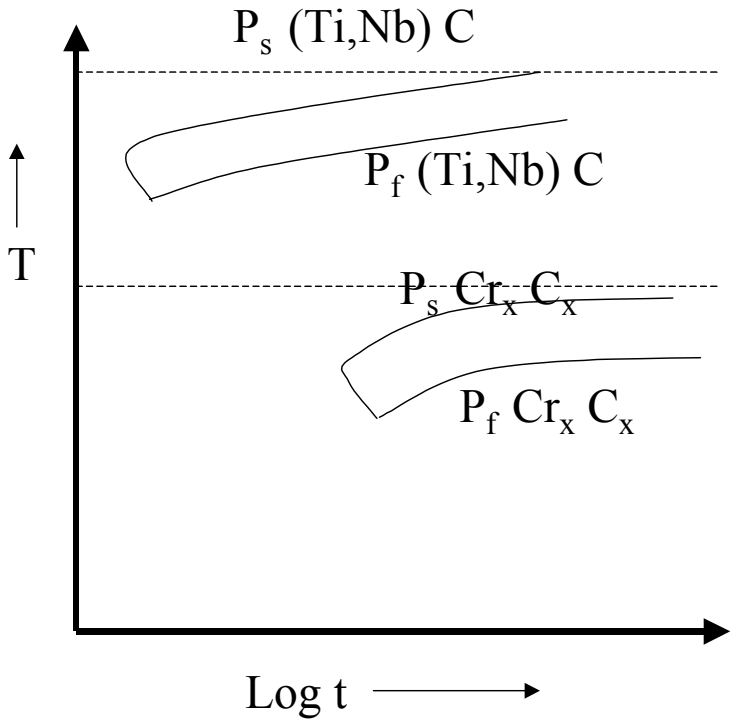

Figure 12 Schematic of a TTT curve demonstrating how additions of titanium and/or niobium form carbides at a higher temperature and shorter time, thus stopping the formation of chromium carbides

stainless steels still suffered from the surface defects that required surface grinding and increased the overall cost of production. In 1990, J.B. Hill studied the surface defects in titanium only stabilized steels[13]. It was found that titanium additions in excess of the solubility at the liquidus temperature precipitated TiN during solidification and that these were the cause of the defects. In order to avoid these defects, titanium levels must be lowered to a point below the solubility limit at the liquidus temperature. At this concentration, the steels cannot be fully stabilized. On this basis, it is clear that the steels must be fully stabilized with both titanium and niobium or surface defects will exist. The most recent stabilization requirement for a single stabilized steel is %Ti = 0.08 + 8(%C + %N)[14]. It has also been published[15] that the total titanium content should be 0.10-0.15% above the stochiometric Ti:C = 4 in single stabilized ferritic stainless steels. The ASTM chemical composition limits for the different types of stabilization in type 409 ferritic stainless steels are given in table 6.

2.4.2 Titanium Plus Niobium Dual Stabilization

In light of the surface quality problems in Ti-only stabilized steels, dual stabilized steels with titanium and niobium were developed. Although the niobium is more expensive than the relative amounts of titanium, the overall production cost can be lowered because of lower surface grinding loss (fig. 13[23]). The addition of titanium plus niobium has also been found to increase the corrosion resistance[16] and increase the formability[17,18]. Current stabilization requirements for dual stabilization are the addition of titanium and niobium such that the total content satisfies the equation (Ti+Nb) = 0.08 + 8 (%C+%N)[14].

Table 6 ASTM standards for stabilization of T409 ferritic stainless steels

UNS Designation	Carbon (wt%)	Nitrogen(wt%)	Titanium/Nionium Requirements
S40910	0.03	0.03	Ti 6x(C+N) min, 0.50 max; Nb 0.17 max
S40920	0.03	0.03	Ti 8x(C+N) min, 0.15-0.50; Nb 0.10 max
S40930	0.03	0.03	Ti+Nb 0.08+8(C+N) min, 0.75 max
S40940	0.06	-----	Nb 10xC, 0.75 max

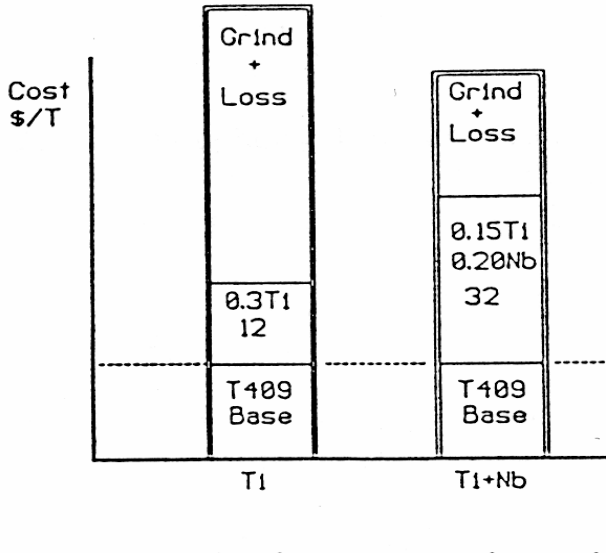

Figure 13 The additional cost of niobium can be offset by the reduction is surface grinding costs

2.4.2.1 Effect of Niobium in Steels

In addition to its stabilization effects, small amounts of niobium in steels have been known to affect both the microstructure and properties. The niobium has been known to increase strength[19,20,21], develop good textures[22], improve surface quality[23], and increase formability[24]. The main benefit of the niobium is its ability to suppress recovery, recrystallization, and grain growth in steels[25]. This occurs from both niobium in solid solution and niobium in precipitates. The topic of niobium in steels has been covered extensively in a review paper by A.J. DeArdo[26].

2.5 Precipitation Prediction Models

2.5.1 Thermocalc Thermodynamic Software

The software program Thermocalc was used to make predictions of the phases present at various temperatures. All of the calculations were made using Thermocalc version N and the Fe-data database. The software is used to make thermodynamic calculations that give the equilibrium concentrations of phases. The software does not take kinetics into account and will therefore predict what the phase balance would be given infinite time.

2.5.2 Solubility Products

Another way to predict the temperatures where carbides will form is to use solubility products. Solubility products give the equilibrium concentration of solute in a given matrix over a range of temperatures. They originate from thermodynamic data that are usually modified to fit experimental data. The solubility of microalloying elements is also dependent on the composition of the steel. Therefore, a separate solubility product should be made for every type

of steel composition, as well as for each phase in a given steel. Since solubility products for 11 percent chromium steels do not exist, the solubility products for low carbon steels were used[27,28]. The solubility products used are as follows:

Table 7 Solubility products for carbides and nitrides in ferrite and austenite

System	Product	Soluble Phase
TiN	Log[Ti][N] = 5.9 – 16586/T	Austenite
	---	Ferrite
TiC	Log[Ti][C] = 2.75 – 7000/T	Austenite
	Log[Ti][C] = 4.4 - 9575/T	Ferrite
NbC	Log[Nb][C] = 3.36 – 7167/T	Austenite
	Log[Nb][C] = 5.43-10960/T	Ferrite
NbN	Log[Nb][N] = 4.04 – 10230/T	Austenite
	Log[Nb][N] = 4.96 – 12230/T	Ferrite

2.6 Precipitate Nucleation and Growth

2.6.1 Homogeneous Nucleation

Most second phases in steels precipitate through a nucleation and growth mechanism. During nucleation, there is an energy balance between the extra energy required to make the particle (surface energy, strain energy) and the energy released by the formation of the more stable second phase. This energy balance can be modeled by equation 2.1:

$$\Delta G = -\frac{4}{3}\pi r^3(\Delta G_v - \Delta G_s) + 4\pi r^2 \gamma_{SL} \qquad \text{(Equation 2.1)}$$

where ΔG_v is the free energy released per unit volume of new phase, ΔG_s is the strain energy associated with the formation of the new phase and γ_{SL} is the surface energy associated with the interface of the two phases. Plotting this equation (Figure 14[29]) demonstrates the dependency of the stability of the new nucleus on nucleus size. As can be seen from the graph, up to a critical nucleus radius ,r^*, the free energy can be decreased by the nucleus dissolving. It therefore requires a fluctuation in the local composition so that a nucleus greater than r^* is formed, which will then grow into a stable particle. As the undercooling is increased, the free energy released from the formation of the particle will increase, thus decreasing the critical nucleus size. In reality, homogeneous nucleation requires large undercoolings and therefore is seldom seen. In most cases, easier heterogeneous nucleation will occur at impurity particles, grain boundaries, or at the free surfaces at higher temperatures.

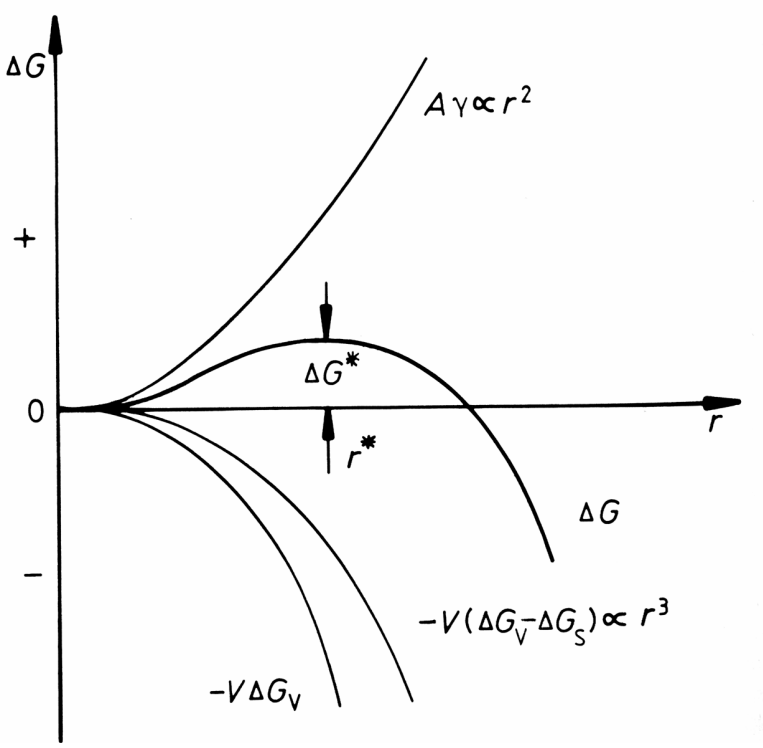

Figure 14 Plot of free energy versus nucleus size for homogeneous nucleation

2.6.2 Heterogeneous Nucleation

To help reduce the energy required for nucleation, a new phase will usually precipitate at some heterogeneity in the matrix. This occurs by using the defect to reduce either the strain energy or the surface energy associated with the formation of a new phase. Assuming a spherical precipitate on a planar boundary, the total change in free energy for the nucleation reaction can be given by:

$$\Delta G = -\frac{4}{3}\pi r^3\left(\Delta G_v - \Delta G_s\right) + 4\pi r^2 \gamma_{P_1P_2} - 2\pi r^2 \gamma_{P_1P_1} \qquad \text{(Equation 2.2)}$$

where ΔG_v is the free energy released per unit volume of new phase, ΔG_s is the strain energy associated with the formation of the new phase and $\gamma_{P_1P_2}$ is the surface energy associated with the interface of the two phases, and $\gamma_{P_1P_1}$ is the surface free energy associated with the boundary. It is clear when comparing equation 2.2 to equation 2.1 from homogeneous nucleation, that the free energy associated with heterogeneous nucleation will always be lower than that from homogeneous nucleation. This is because the final term in the equation represents the free energy gained from the area of the defect that is eliminated. Also, the strain energy term is also often smaller in the case of heterogeneous nucleation due to the presence of a large number of dislocations and vacancies at structural heterogeneities.

2.6.2.1 Examples of Heterogeneous Nucleation in Ferritic Stainless Steels

As previously mentioned, most second phases will nucleate heterogeneously in steels. In ferritic stainless steels, there have been several observations of this phenomenon including the epitaxial precipitation of (Ti,Nb)C on TiN[30,31] and the formation of austenite at grain boundaries[32]. In the case of epitaxial precipitation of carbides on TiN, the energy required for

nucleation is further lowered by a low energy semi-coherent interface between the TiN and the (Ti,Nb)C. The lattice misfit between the two particles is between 2.5 percent (TiN-TiC) and 5 percent (TiN-NbC). Consider the surface free energy in two dimensions if the particle were to nucleate homogeneously or heterogeneously on the TiN (fig. 15). Considering both precipitates in the matrix, the total surface energy would be as follows:

$$\Delta G_{surf} = 4L * \gamma_{TiN/Matrix} + 2(L+t) * \gamma_{(TI,Nb)C/Matrix} \quad \text{(Equation 2.3)}$$

where γ is the surface free energy per unit length. By precipitating epitaxially as shown in Figure 15, the total surface energy will be:

$$\Delta G_{surf} = 3L * \gamma_{TiN/Matrix} + (L+2t) * \gamma_{(TI,Nb)C/Matrix} + L * \gamma_{TiN/(Ti,Nb)C} \quad \text{(Equation 2.4)}$$

By setting the two equations equal to each other, it can be deduced that the surface energy for epitaxial precipitation will be lower when:

$$\gamma_{TiN/(Ti,Nb)C} < \gamma_{TiN/Matrix} + \gamma_{(Ti,Nb)C/Matrix} \quad \text{(Equation 2.5)}$$

Therefore, the total surface energy in heterogeneous nucleation of carbides will be about one half that of homogeneous nucleation.

It has also been shown that austenite in steels tends to nucleate on the ferrite grain boundaries and other structural heterogeneities. In this specific case of heterogeneous nucleation, the austenite uses the energy from the grain boundary that is destroyed to decrease the nucleation barrier. Once again, comparing the surface energy of the austenite in the matrix and the austenite on the grain boundary (fig 16), it is clear that the total surface free energy will be lower if the austenite nucleates on the grain boundary. There are also other factors such as segregation of carbon to the grain boundary and a decrease in strain energy for austenite formed at the grain boundary that will aid in the grain boundary nucleation of austenite.

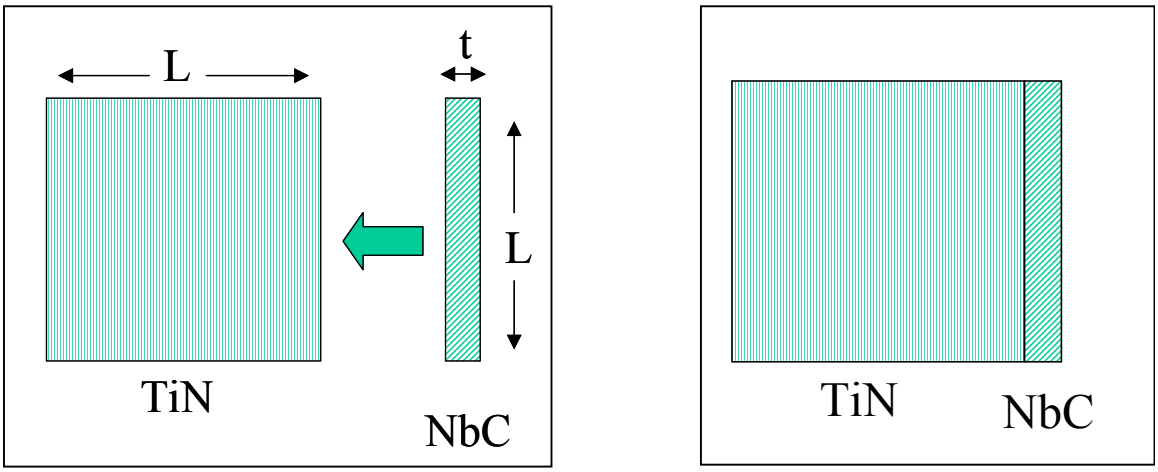

Figure 15 Diagram showing the (Ti,Nb)C independent from the TiN (left) and NbC epitaxially precipitated on the TiN (right)

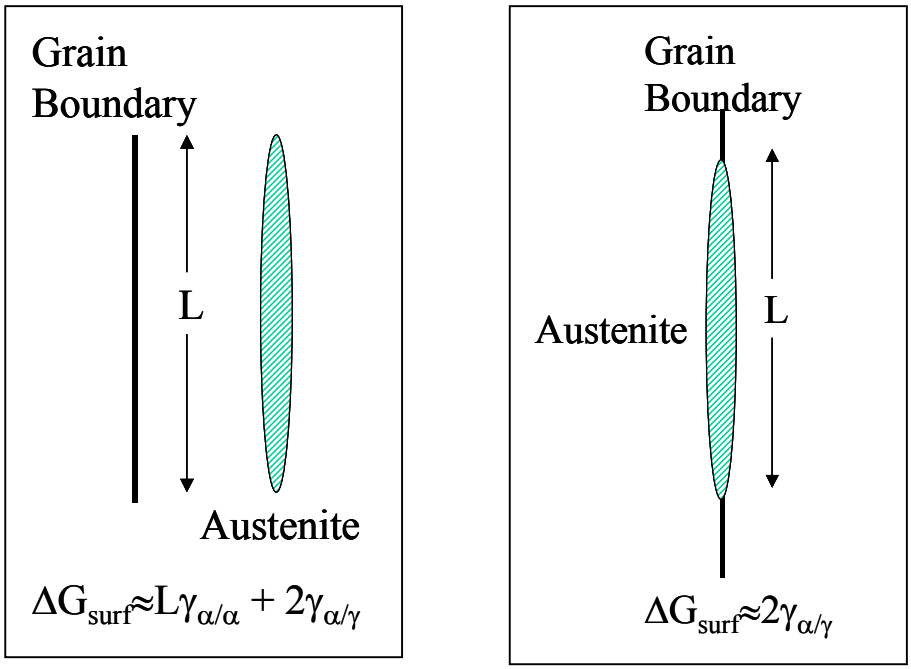

Figure 16 Austenite nucleated in the matrix (left) will have a higher surface free energy than austenite nucleated on the grain boundary(right)

2.6.3 Precipitate Growth (Ostwald Ripening)

Precipitate growth at the expense of the smaller precipitates becomes an important phenomena during continuous cooling deformation testing, which will we be described further in section 4.5.1. During the early stages of precipitation, nucleation and growth will occur simultaneously until all of the carbon is taken out of solution. Once the carbon is removed from solution, the nucleation will stop and the larger carbide particles will begin to grow at the expense of the smaller particles in a process known as Ostwald ripening. Ostwald ripening is the coarsening process of second phase particles when the matrix concentration of solute remains static, i.e., there is no dissolution and re-precipitation of particles. The driving force for the ripening process is the reduction of surface area between the particles and the matrix. The surface area of a fewer number of large particles will be much smaller than the surface area of several fine particles. This can be compared to the driving force for grain growth. However, in contrast to grain growth, the particles are usually separated by considerable distances. Therefore, a diffusion mechanism must be taken into account. The Thomson-Freundlich[33] equation relates the local solubility at the matrix-particle interface to the size of the particle.

$$\ln\left(\frac{S_r}{S}\right) = \frac{2\Omega\sigma}{RTr} \qquad \text{(Equation 2.6)}$$

where S_r is the solute content in equilibrium with a particle of radius r, S is the true equilibrium solubility (with an infinitely large particle), Ω is the molar volume of precipitates, σ is the interfacial surface energy between the particle and the matrix, R is the gas constant, and T is the temperature in Kelvin. This equation demonstrates that the local solute content around larger particles will be lower than the local solute content around smaller particles, setting up a

diffusion gradient. The rate of Ostwald ripening will therefore depend on the diffusion of solute elements and the dominant diffusion mechanism.

2.7 Orientation Relationships

Through TEM investigation of the orientation relationship between the carbide and the matrix, it is possible to determine if the carbide formed in ferrite or austenite. This is important in determining the temperature where the carbide forms, and also in determining the presence of austenite in the temperature range where the precipitation occurs. The carbide will conform closely to either the Kurdjumov-Sachs orientation relationship or the Baker-Nutting Orientation relationship as described in the following sections.

2.7.1 Kurdjumov-Sachs Orientation Relationship

The Kurdjumov-Sachs orientation relationship is used to describe the orientation between an FCC lattice and a BCC lattice. When this occurs, the close packed planes between the two crystal structures will be aligned as shown in Figure 17 so that:

$$(110)_{BCC} \parallel (111)_{FCC}$$

$$[111]_{BCC} \parallel [110]_{FCC}$$

where (110) is the close packed plane in BCC and (111) is the close packed plane in the FCC. This orientation relationship has been observed at ferrite/austenite grain boundaries. This orientation relationship can also be used to indicate the precipitation of carbides in the austenite phase. Carbides will initially form in austenite with FCC lattice parallel to that of the FCC austenite:

$$(100)_{MC} \parallel (100)_{\gamma}$$

$$[010]_{MC} \parallel [010]_{\gamma}$$

The austenite/ferrite boundary will then move past the particle, leaving the particle with the K-S relationship with respect to the matrix.

2.7.2 Baker-Nutting Relationship

The Baker-Nutting orientation relationship describes the relationship between a carbide particle and the matrix when the carbide precipitates in the ferrite. The B-N relationship is shown schematically in Figure 18 and can be shown as:

$$(100)_{MC} \parallel (100)_{\alpha}$$

$$[100]_{MC} \parallel [110]_{\alpha}$$

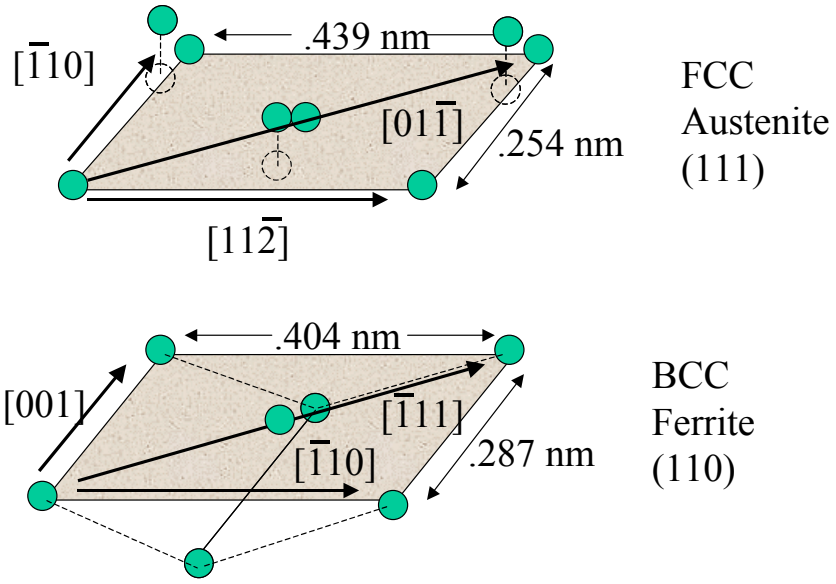

Figure 17 Schematic showing the parallel planes and directions in the Kurdjumov-Sachs orientation relationship between ferrite and austenite

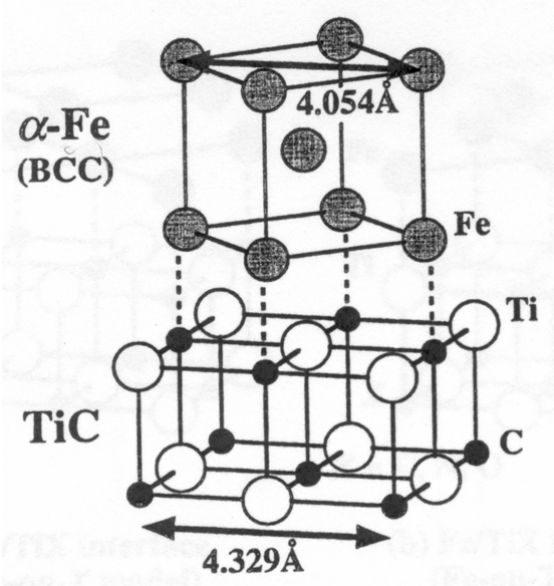

Figure 18 Schematic of the Baker-Nutting Orientation Relationship between a titanium carbide particle and the ferrite matrix

2.8 Precipitation Strengthening

In type 409 ferritic stainless steels, precipitation strengthening does not play a significant role in the properties of the final product. However, when precipitation first occurs during continuous cooling, the precipitates temporarily have a sufficiently small size and large volume fraction to cause a detectable increase in the strength. This is used in continuous cooling deformation testing to detect the precipitation start temperature, as shown in Section 4.5.1. For this reason, the fundamentals of precipitation strengthening will be discussed.

Precipitation strengthening derives its origins from the ability of precipitates to block the movement of dislocations. There are two ways for a dislocation to move past a particle, a Friedel cutting mechanism or an Orowan-Ashby looping mechanism. When carbide particles form in the steels, they are generally non-deformable particles since they are much harder than the ferrite matrix. Therefore, dislocations must adopt a looping mechanism as shown in Figure 19[34] to bypass the particles. In an attempt to predict the shear stress necessary to bypass a particle, there have been several modifications[35,36] to the original equation proposed by Orowan[37] in 1954 that lead to equation 2.7 below:

$$\sigma = \frac{5.9\sqrt{f_v}}{r} \ln\left(\frac{r}{2.5x10^{-4}}\right) \qquad \text{(Equation 2.7)}$$

where r is the radius of the particle and f_v is the volume fraction of particles. The derivation of equation 2.7 has been summarized in several texts[38,39]. This shear stress required to move a dislocation past a particle is calculated by assuming a field of randomly distributed, hard,

nondeformable particles. It is clear from this equation that the greatest strengthening will occur from a fine dispersion of small particles.

During precipitation, both r and f_v will increase until all of the carbon has precipitated out. Therefore, the strengthening will increase up until the end of precipitation. After all of the carbon is removed from solution, the larger precipitates will tend to grow at the expense of the smaller precipitates as discussed in Section 2.6.3. As the larger precipitates coarsen and the smaller precipitates dissolve, the amount of strengthening will decrease until the effect of the particles becomes negligible.

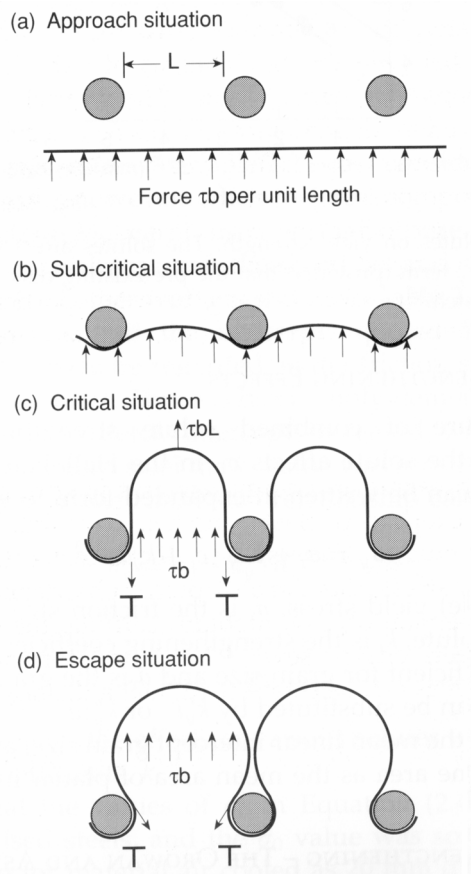

Figure 19 Diagram of a dislocation moving past non-deformable particles using the Orowan looping mechanism

3.0 STATEMENT OF OBJECTIVES

The objective of this investigation was to study the fundamental metallurgy of both single stabilized (Ti-Only) and dual stabilized (Ti+ Nb) type 409 ferritic stainless steels in order to understand the differences in behavior of the two systems.

The precipitation studies were designed with two specific goals in mind. The first goal was to characterize the precipitates in the as-received transfer bar. The second goal was to study the dissolution and re-precipitation of the TiC and (Ti,Nb)C particles during isothermal reheating and continuous cooling. From this data, it is possible to infer when the carbon is in solution and when the carbon is tied up in precipitates at high temperatures.

The austenite formation studies were designed to give a better understanding as to the kinetics of the austenite transformation and the mechanisms by which the austenite forms. Finally, the amount of carbon in the austenite has been studied in an attempt to determine the effects that carbon in solution could have on the kinetics of the austenite formation.

4.0 EXPERIMENTAL PROCEDURE

4.1 Chemical Compositions

For the purpose of this research, two steels were chosen to demonstrate the fundamental differences between single stabilized Ti-Only type 409 and dual stabilized (Ti+Nb) type 409 ferritic stainless steels. The aim chemistries were to be the same in all elements except for the titanium and niobium concentrations. The actual samples obtained were from commercially produced hot band so the chemistries could not be controlled. It should be noted that the dual stabilized steel had much higher carbon, nitrogen, titanium, and niobium content in the dual stabilized steel were significantly higher than in the single stabilized steel and hence precipitation and austenite formation could be significantly affected. The steel compositions, along with the aim composition, are given below in Table 7.

Table 8 Chemical compositions of experimental steels used in this research

Steel Type	**C**	**N**	**Ti**	**Nb**	**Cr**	**Ni**	**Mn**	**Si**
Aim (Ti-Only)	0.008	0.008	0.20	0.0	11.0	0.10	0.30	0.40
Ti-Only	0.0091	0.0081	0.22	0.007	11.18	0.050	0.27	0.39
Aim (Ti+Nb)	0.008	0.008	0.10	0.10	11.0	0.10	0.30	0.40
Ti + Nb	0.015	0.013	0.20	0.150	11.07	0.240	0.31	0.45

4.2 Material Processing

The initial as-received material was transfer bar 25.4cm thick. The slabs were continuously cast and then cooled to room temperature. The slabs were then reheated to 1250 °C

for about 1 hour before hot rolling. Once in the hot rolling mill, the slabs went through the roughing stands before a sample was sheared and allowed to air cool to room temperature from approximately 1050 °C.

4.3 Experimental Equipment

4.3.1 Theta Dilatometer

A Theta Dilamatic IIe dilatometer was used in this research because of its computer-controlled furnace with a semi-enclosed sample chamber. This furnace was utilized for heating and cooling experiments where the heating and cooling rates needed to be controlled. The furnace uses a resistance-heating element that can obtain heating rates of up to 10 °C per second. This furnace is interfaced to a PC through the serial port, allowing for two-way communication between the computer and the temperature controller. This allows the computer to record the temperature data from the controller, as well as continuously change the sample set point temperature and heating rate. The sample temperature is monitored through a k-type thermocouple spot welded to the surface of the sample. The sample is contained in a semi-enclosed quartz tube. The quartz tube had an opening at one end to allow the sample to be removed quickly and water quenched. Argon flowed into the quartz tube at the closed end, across the sample, and out the open end of the tube. Increasing the argon flow across the sample could also be used to obtain higher cooling rates.

4.3.2 MTS Hot Compression Testing System with Open-Air Furnace

In cases where deformation was necessary, an MTS hot compression testing system was used (fig 20). Standard sample size is a cylinder 19 cm in height and 12.7 cm in diameter. The sample temperature is measured by a k-type thermocouple with an exposed junction that is

inserted 1 mm into the sample at the midpoint of the height. A dual element thermocouple was used so that one reading goes to the temperature controller and one reading goes to the PC for data acquisition. An open-air furnace with Sylvania 1200 W halogen quartz infrared bulbs is used to heat the sample. Figure 21 shows an image of the furnace mounted on the MTS. The capabilities of the furnace are 1225 °C maximum temperature and 10 °C per second heating rate. The compression unit is hydraulically driven and controlled by an MTS 458.20 Microconsole. The load cell installed on the unit is a MTS model 661.2 with a maximum load capacity of 200 kN. Swapping cards on the Microconsole can change the displacement and load ranges. The load cards available have a range from 0-20 kN up to 0-200 kips. The load range chosen was 0-5 kips. The displacement chosen was 25.4 mm of displacement. The maximum displacement is 127 mm and the minimum displacement range is 12.7 mm. The strain rate is variable from 0.001 sec^{-1} up to 10 sec^{-1}. A PC was used to record the data, load, position, and temperature.

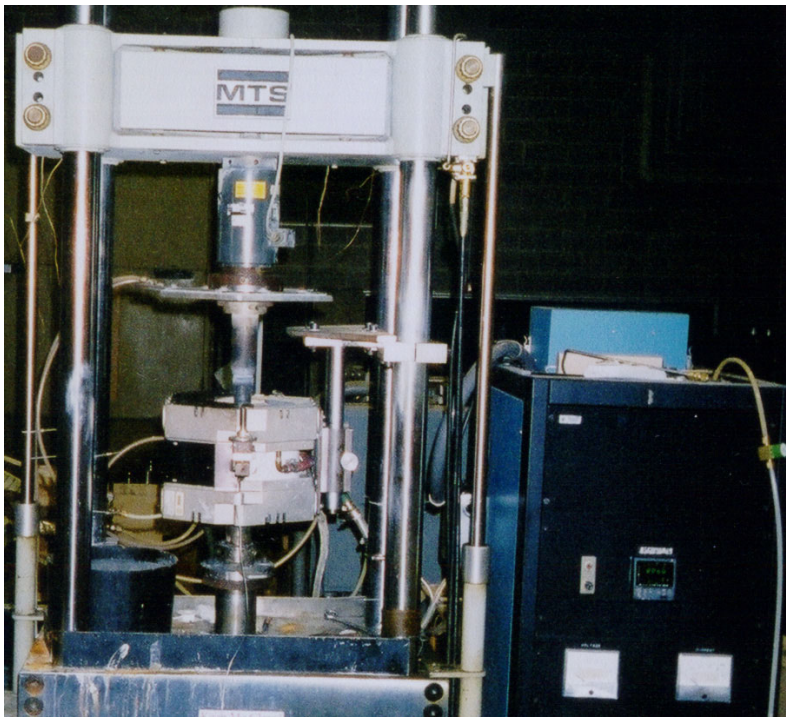

Figure 20 Picture of the MTS hot compression system at the University of Pittsburgh

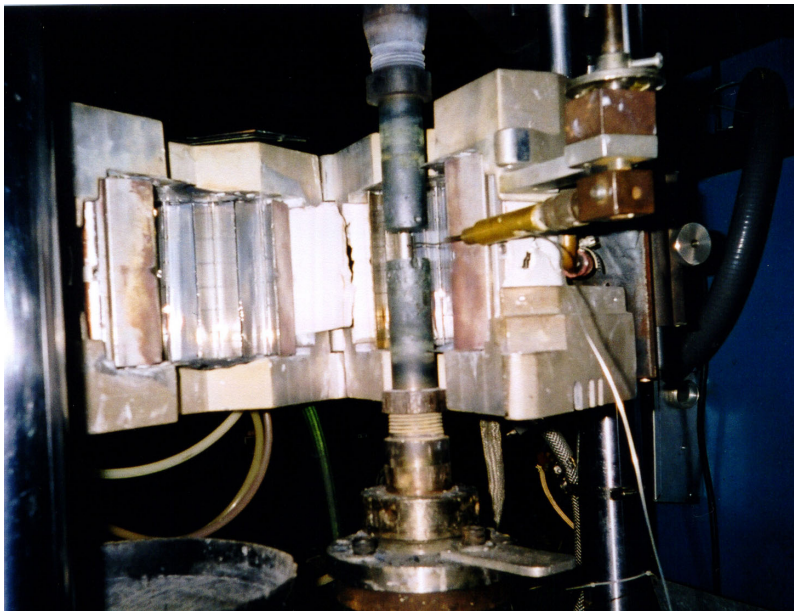

Figure 21 Picture of the infrared furnace used to heat the samples in the MTS hot compression system

4.4 Precipitate Dissolution Studies

The first step in this research was to determine the temperatures at which the carbides dissolved and the carbon was released back into the matrix. Initially, samples were obtained that had been previously heat treated for varying times in the temperature range of 800 to 1200 °C. A schematic of these treatments is given in Figure 22[40]. These specimens were analyzed using a point count method to determine the volume fraction of free standing precipitates. Next, since the epitaxial precipitates did not dissolve at 1200 °C, more samples were reheated to increasingly higher temperatures. Samples were held for 30-90 minutes from 1200-1300 °C. The samples were then water quenched and analyzed on the Scanning Electron Microscope and the Transmission Electron Microscope to locate and identify precipitates.

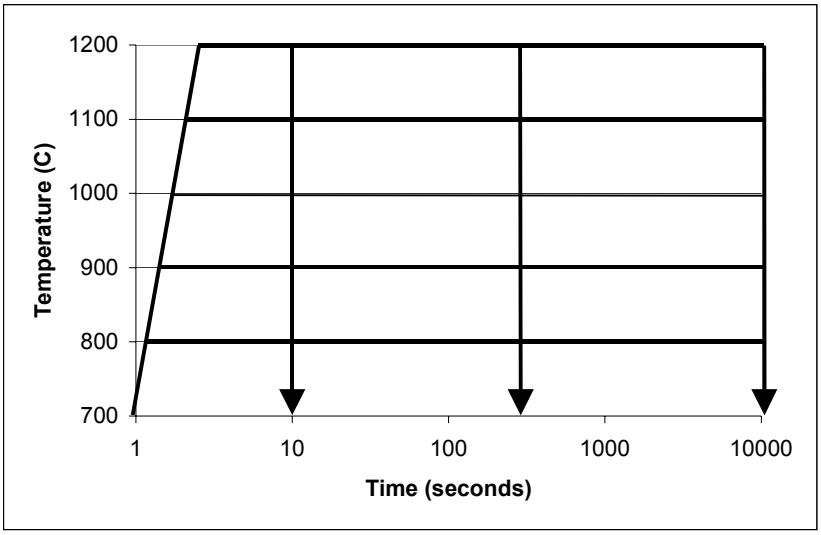

Figure 22 Heat treatments performed by Kappeler and Schaupp to measure austenite volume fractions

4.5 Precipitation Studies

4.5.1 Continuous Cooling Deformation (CCD) Testing

Continuous Cooling Deformation testing is a technique developed by Hanzaki[41] et al. that uses load data to identify microstructural changes in the steel. In CCD testing, a sample is slowly deformed ($\dot{\varepsilon} = 0.001$ sec $^{-1}$) while being cooled at a constant cooling rate. In the absence of any microstructural changes, the load data will show a logarithmic trend line when plotted against time. However, changes in the microstructure, such as a phase transformation or precipitation, will cause an inflection in the load. Figure 23 shows a log[load] vs. temperature curve for low carbon steel that is cooled through the austenite to ferrite transition. Because the ferrite is much softer than austenite, there is a decrease in the load as the transformation progresses. Once the sample is 100 percent ferrite, the trend will again become linear.

This testing method was applied to precipitation testing in T409 ferritic stainless steel by Moses[42]. Moses et al determined that the first deviation from the expected flow curve is due to the start of precipitation and the second deviation can be interpreted as the end of precipitation. To determine the first deviation, the slope of the log load vs. temperature line was averaged over 5 data points (5 sec or 5 °C at 1°C/sec) and the inflection point was taken to be when the slope deviated by more than 5 N/°C. Using these data points, a continuous cooling precipitation curve can be constructed.

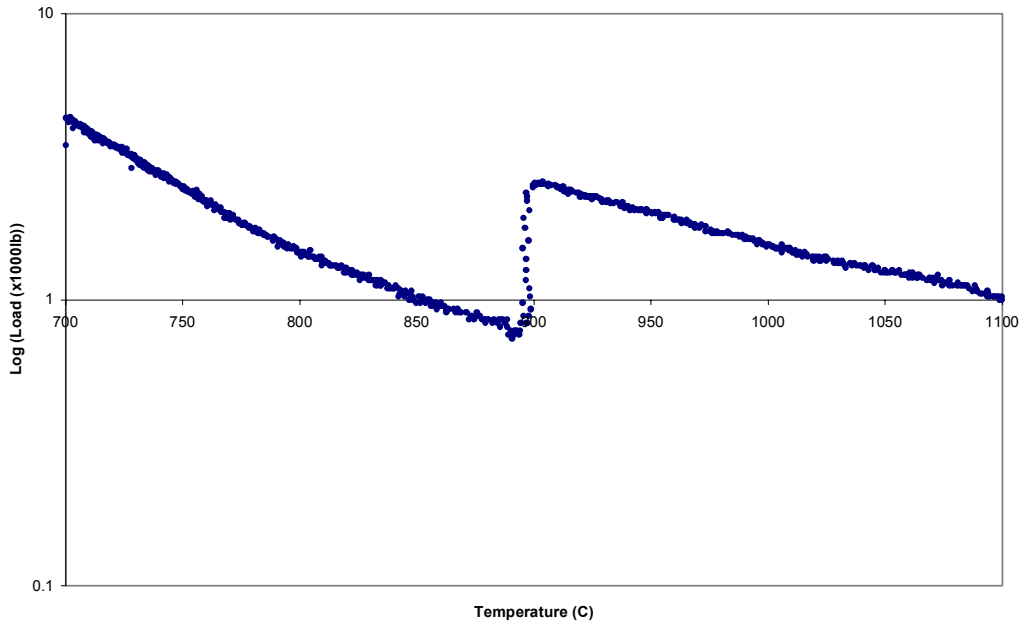

Figure 23 Continuous cooling deformation results showing the austenite to ferrite transformation in an IF steel

4.5.2 Precipitation Testing

Another method used to determine the precipitation start and precipitation finish temperatures was to heat treat the samples in the dilatometer furnace and then water quench from different temperatures during cooling. These samples were then analyzed in the SEM and TEM to assess the presence or absence of precipitates.

4.6 Microanalysis of Samples

Several types of microscopy were performed to locate, identify, and quantify the microstructure of the samples. Many different microscopes were used, ranging from optical microscopy to Transmission Electron Microscopy. Analysis of small particles can often prove difficult. However, previous work[43,44] has shown that a combination of different types of

electron microscopes and energy dispersive spectroscopy can provide valuable insight into precipitation behavior.

4.6.1 Sample Preparation

4.6.1.1 Optical Microscopy

To prepare samples for optical microscopy, samples were sectioned using a Buehler Isomet 1000 diamond cutting wheel and were then hot-mounted in Bakelite compound using a Buehler Pnumet I mounting press. The samples were then ground using silicon carbide paper down to 600 grit. After polishing with 1.0 and 0.05 μm alumina on a polishing cloth, the samples were etched using Villela's etchant which consists of:

1000 ml ethanol

50 ml hydrochloric acid

30 g picric acid

To help distinguish between ferrite and martensite, some samples were also additionally etched using Kallings #1 etchant. Kallings #1 etchant is usually used in duplex stainless steels to preferentially attack the martensite. Kalling's #1 solution consists of:

1.5 g cupric chloride

33 ml ethanol

33 ml distilled water

33 ml hydrochloric acid

4.6.1.2 Transmission Electron Microscopy (TEM)

Thin foil preparation involves sectioning the samples, mechanical or chemical thinning, and electropolishing. Samples were first sectioned to 1.25 mm using a Buehler Isomet 1000 diamond cutting wheel. The thin samples were then attached to a larger steel block using a hot plate and wax. Once the sample was mechanically ground on one side using 320, 400 and 600 grit silicon carbide paper the foil was again placed on the hot plate to melt the wax. The sample was flipped over and then mechanically ground on the opposite side. After the sample was sufficiently thin and rough ground using 600 grit paper, the wax was dissolved using acetone. TEM foils were then punched into 3 mm discs and elecropolished until perforation using a twin-jet electropolisher. Finally, the samples were cleaned using a three step ethanol cleaning process to remove all residues on the sample.

4.6.1.3 Scanning Electron Microscopy (SEM)

Samples for analysis on the SEM were prepared either as optical microscopy bulk samples or TEM thin foils. Most samples analyzed on the SEM were prepared as TEM thin foils even if they were not going to be analyzed in the TEM. There are three reasons for routinely preparing TEM foils for the SEM. The first is because the TEM foil preparation keeps the sample very clean which helps resolve small particles. Second, the twin-jet electopolisher tends to leave carbides and nitrides on top of the surface, facilitating good images and analysis of the particles. The final reason why TEM foils were usually prepared for SEM analysis was that it always left the option open for further analysis on the TEM.

4.6.2 Micro-Analysis Instruments

Optical micrographs were captured using a Sony digital camera attached to a Nikon Microscope. Bioquant image analysis software was utilized to save the images on the computer in jpeg format. To analyze larger precipitates and grain structure, a Philips XL30 FEG SEM was used. Typical parameters for the SEM would be 15 kV and spot size 3. Elemental analysis was done using an EDAX CDU LEAP detector. Samples were in focus at a 10 mm working distance for all images and analyses. All SEM images were captured in TIFF compressed format. For further analysis of small precipitates and to obtain crystallographic data, a transmission electron microscope (TEM) and a scanning transmission electron microscope (STEM) were used. TEM and STEM work were done on a Jeol 200CX and JEOL JEM-2000FX, respectively. Both the TEM and the STEM use tungsten filaments operated at 200 kV, 118 μA, and a spot size of 2. All images and diffraction patterns were photographed using 10.2x 5.2cm negatives at various exposure times. The STEM is also equipped with a LINK Systems EDXS that is used to determine the composition of small particles. The two electron microscopes complemented each other, with the 200CX producing better resolution images and diffraction patterns and the 2000FX giving elemental data.

5.0 RESULTS

5.1 Thermodynamic Predictions

The Thermocalc® thermodynamic software package gives very different predictions for the single and dual stabilized steels. In the dual stabilized steel, Thermocalc® treats the TiN and (Ti,Nb)C independently. However, in the single stabilized steel, the software gives results for only one Ti(N,C) particle. Figures 24 through 26 present the volume fraction and composition of the precipitates predicted for the dual stabilized steel. Figures 27 and 28 show the volume fraction and composition of the precipitates predicted for the single stabilized steel.

The results from solubility products are summarized in Figures 29 and 30. In the single stabilized steel, the solubility products from HSLA steels predict a precipitation start temperature of 1080 °C. The dual stabilized steel, considering only the individual TiC and NbC, is predicted from solubility products to precipitate TiC at 1110 °C and NbC at 1080 °C.

In summary, the results from Thermocalc and solubilitity products are as follows. Thermocalc predicts TiN forming in the liquid and NbC precipitation at 1200 °C. In contrast, Thermocalc calculates that a complex Ti(C,N) precipitate will form in the single stabilizing steel, with most of the carbon entering the precipitate below 1200 °C. The solubility products both predicted a lower precipitation temperature than Thermocalc. The TiC in the single stabilized steel is expected to form below 1180 °C and the NbC in the dual stabilized steel is expected to form at about 1210 °C, which is only 30 °C higher than the TiC in the single stabilized steel.

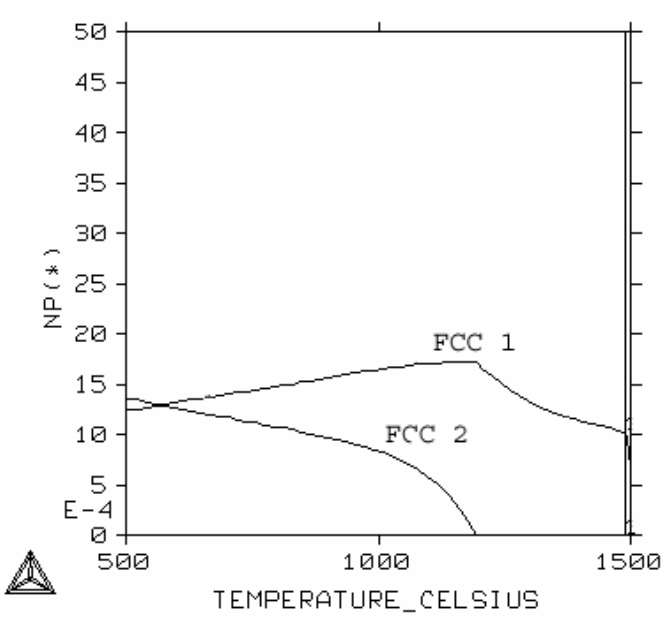

Figure 24 Volume fraction of precipitates predicted by Thermocalc® for the dual stabilized T409

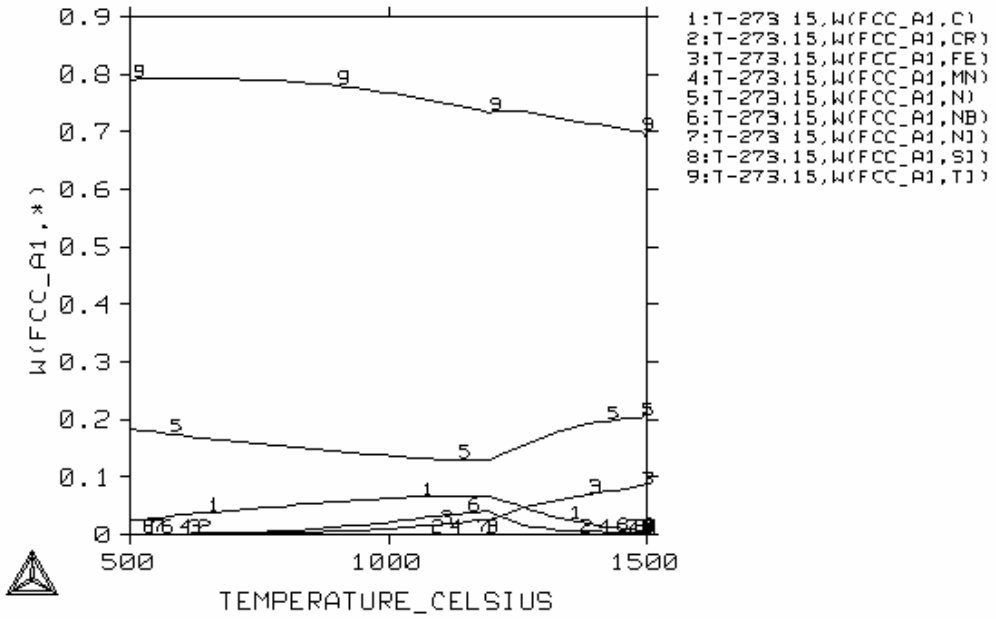

Figure 25 Predicted composition of phase FCC 1, which is mostly TiN

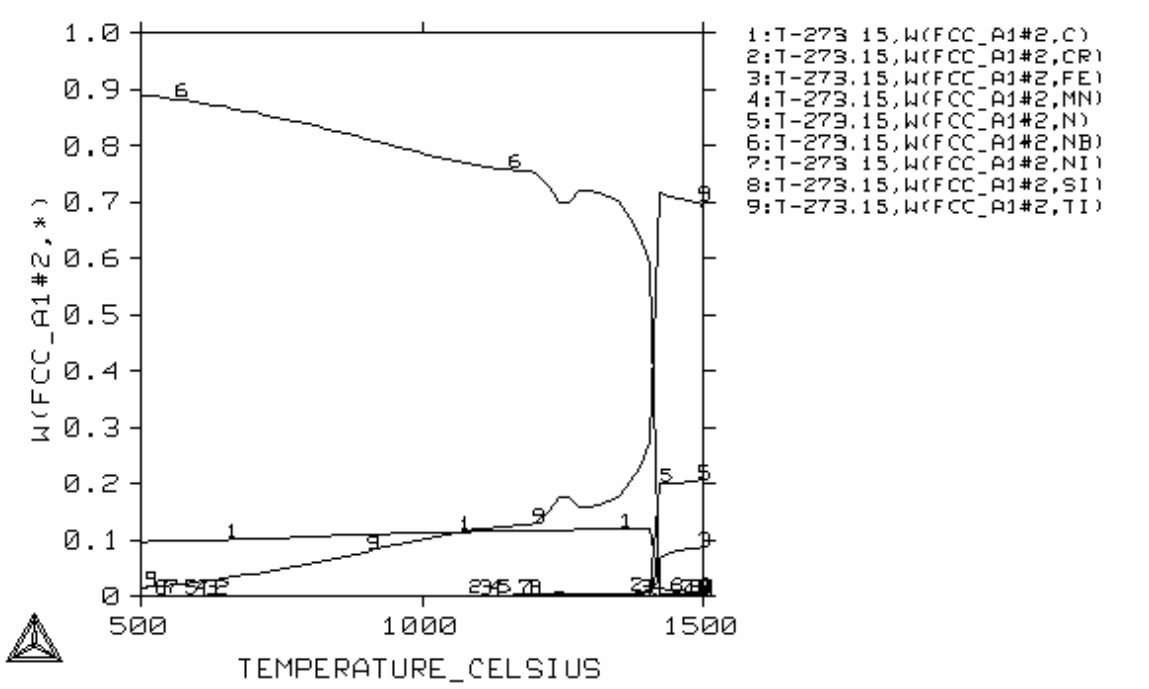

Figure 26 Predicted composition of phase FCC 2 , which is mostly NbC

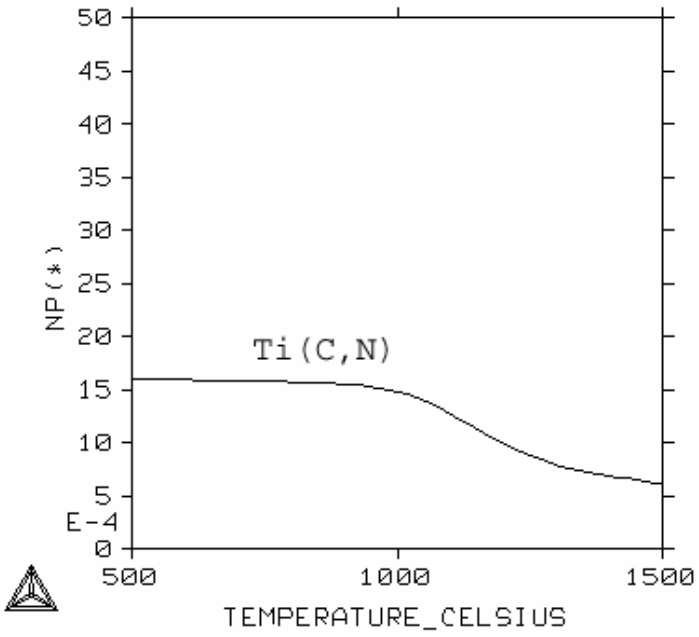

Figure 27 Volume fraction of precipitates predicted by Thermocalc® for the single stabilized T409

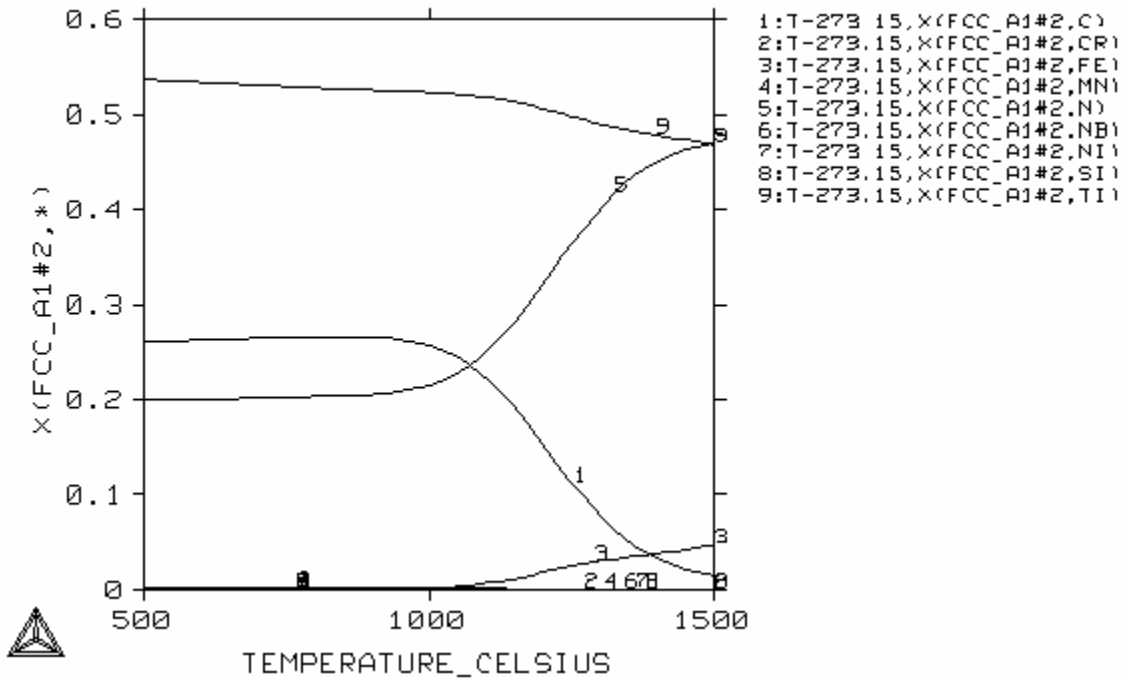

Figure 28 Predicted chemistry of the Ti(C,N) particle for the dual stabilized steel from Thermocalc®

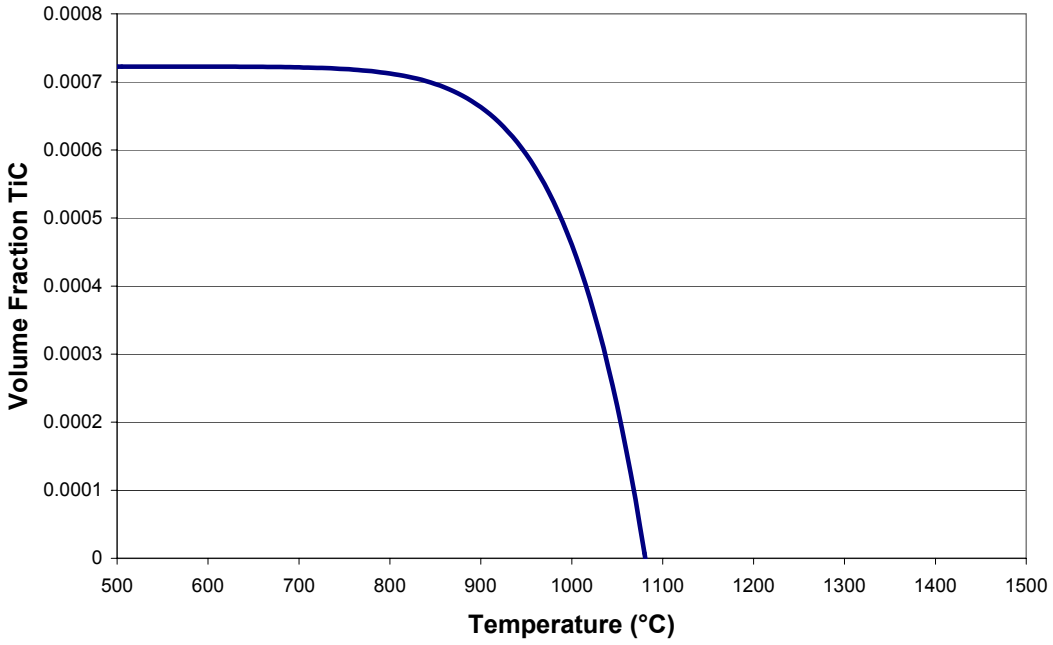

Figure 29 Volume fraction of TiC in the single stabilized T409 as predicted by HSLA solubility products

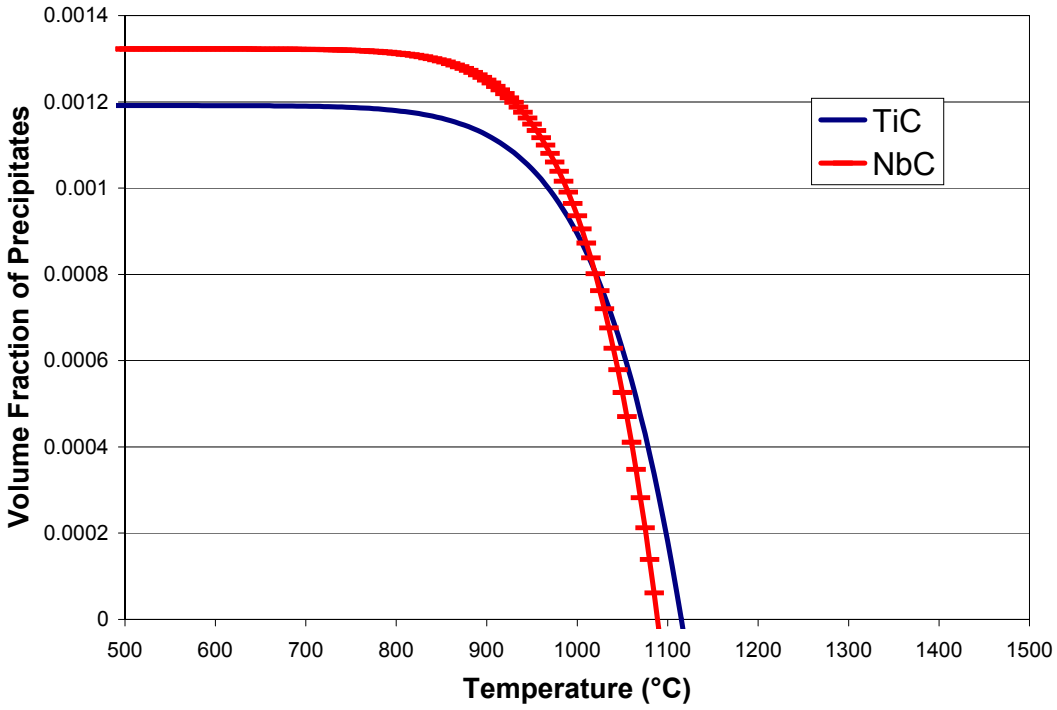

Figure 30 Volume fractions of TiC and NbC in the dual stabilized T409 as predicted by HSLA solubility products

5.2 As-Received Conditions

5.2.1 Phase Balance / Grain Structure

The starting transfer bar material consisted of a fully ferrite matrix in both steels. Both steels showed an equiaxed grain structure with a grain size of 150 μm. Since the transfer bar was allowed to air cool from 1000 °C, we would expect a fully recrystallized, 100 percent ferrite matrix. Optical micrographs of the two steels as-received are shown in Figure 31.

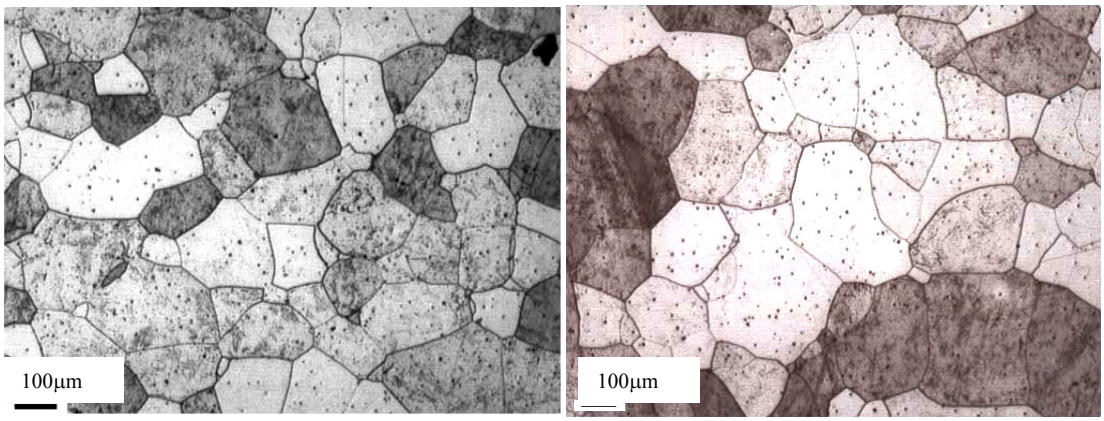

Figure 31 Optical micrographs of as-received samples. The single stabilized steel is on the left and the dual stabilized steel is on the right.

5.2.2 Precipitates

5.2.2.1 Size, Location, Composition

The as-received samples showed a marked difference in the carbide precipitates present. Both steels showed large TiN particles, ranging in size from 0.5 to 5 μm. On the surface of the TiN were epitaxial precipitates. In the single stabilized steel, these were small titanium carbides. An image of the TiN particle is shown in Figure 32 along with the EDS spectrum of the

TiN(Figure 33) and the TiC(Figure 34). In the dual stabilized steel, there was a greater amount of epitaxial precipitation of (Ti,Nb)C on the TiN. An image of an as-received TiN particle is shown in Figure 35 along with spectrum of the TiN(Figure 36) and (Ti,Nb)C (Figure 37). In the case of the dual stabilized steel it is difficult to determine whether the epitaxial precipitates are NbC or a complex (Ti,Nb)C. This is because there is always some interaction between the beam and the TiN particle on the SEM and the TiN particles are usually too large for the beam to pass through on the TEM. However, it does appear that the epitaxial particles are a combination (Ti,Nb)C based on EDS data from the STEM where one small epitaxial particle was identified.

Both steels also contained free standing carbides. In the single stabilized steel, small (200-500 nm) TiC precipitates were found mostly on grain boundaries and prior grain boundaries, as shown in Figure 38, which is a combination of several SEM images. There are some precipitates on the grain boundary in the bottom left of the image and there are also particles that show the grain boundaries before they moved in the central left. The large particle in the center of the image is a non-metallic inclusion, probably from steelmaking. There were also very few eutectic-like titanium carbide precipitates scattered in the matrix (Figure 39).

In the dual stabilized steel, the free standing (Ti,Nb)C precipitates were more homogeneously distributed around the sample, not just on the grain boundaries. The particles were also larger, ranging up to 1 μm in size. Figure 40 shows the matrix of the sample with several (Ti,Nb)C as well as TiN. All of the analyzed particles were a combination, (Ti,Nb)C. There were no TiC or NbC precipitates found in any of the dual stabilized samples.

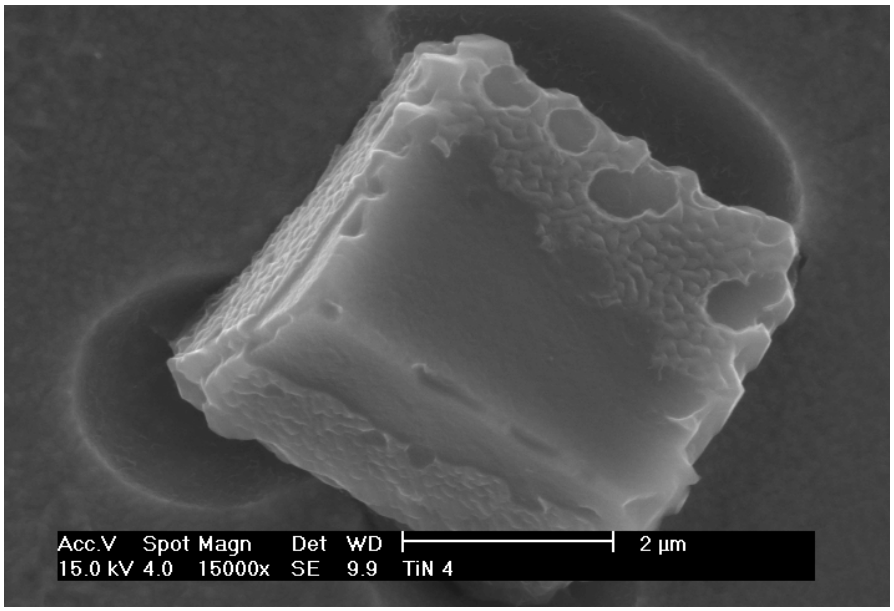

Figure 32 SEM image of a large TiN particle with epitaxial TiC particles

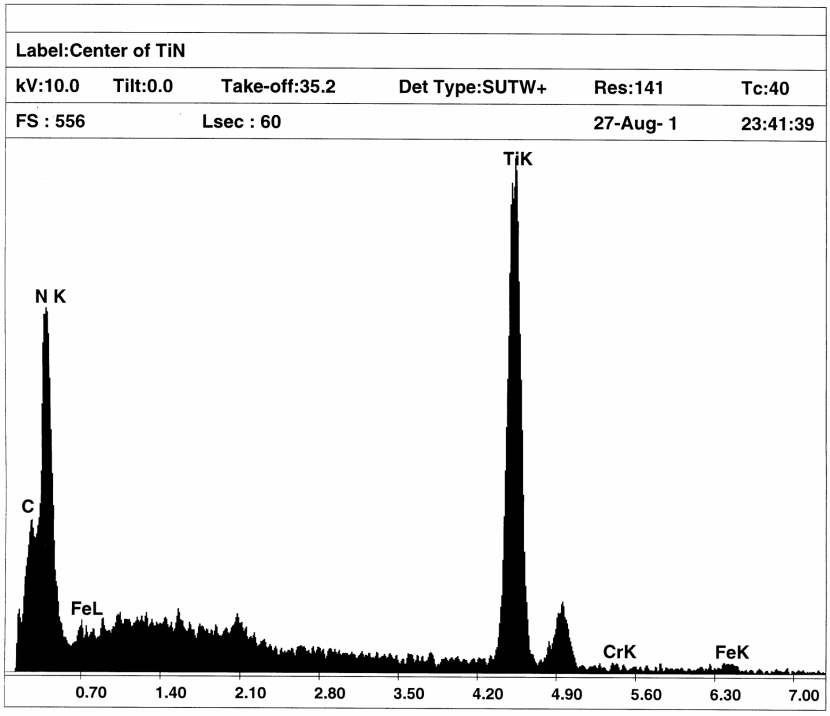

Figure 33 EDS analysis of center of TiN in single stabilized steel

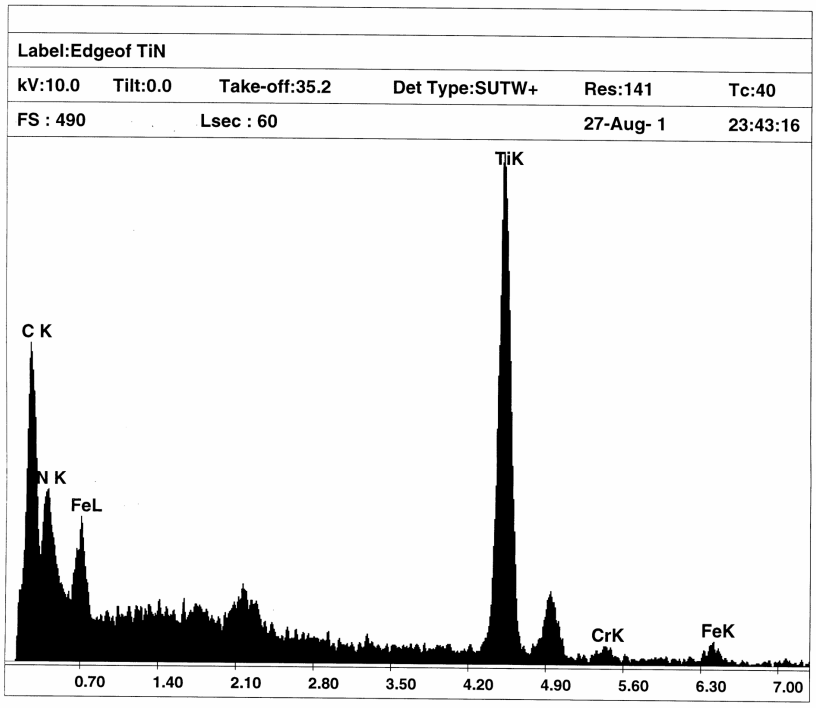

Figure 34 EDS analysis of edge of TiN particle in single stabilized T409 showing epitaxial TiC

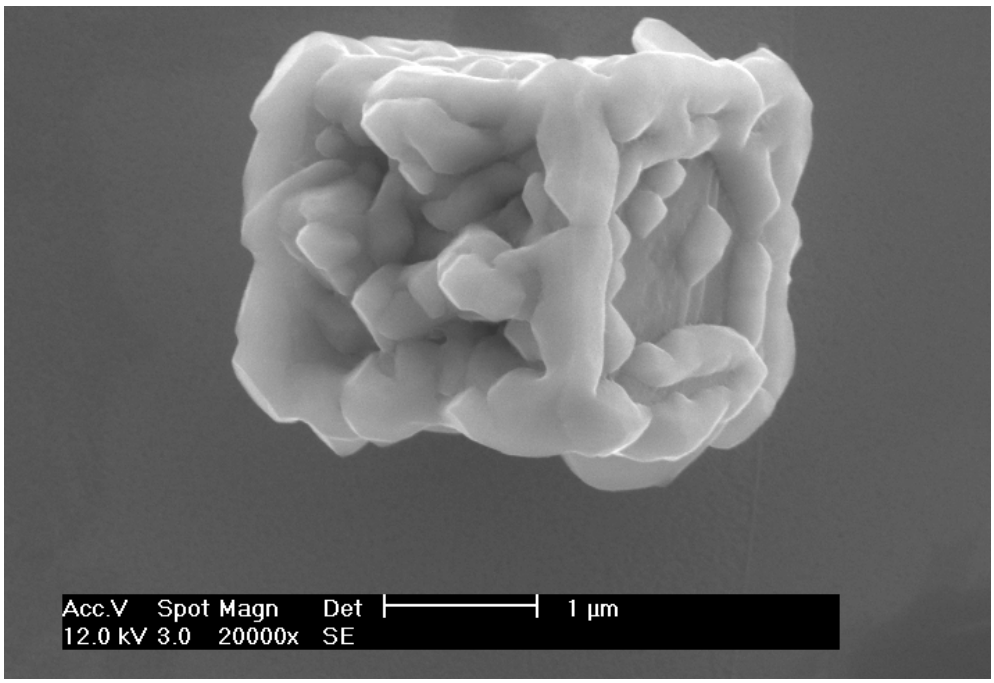

Figure 35 SEM image of a TiN particle containing epitaxial (Ti,Nb)C in the as-received dual stabilized steel

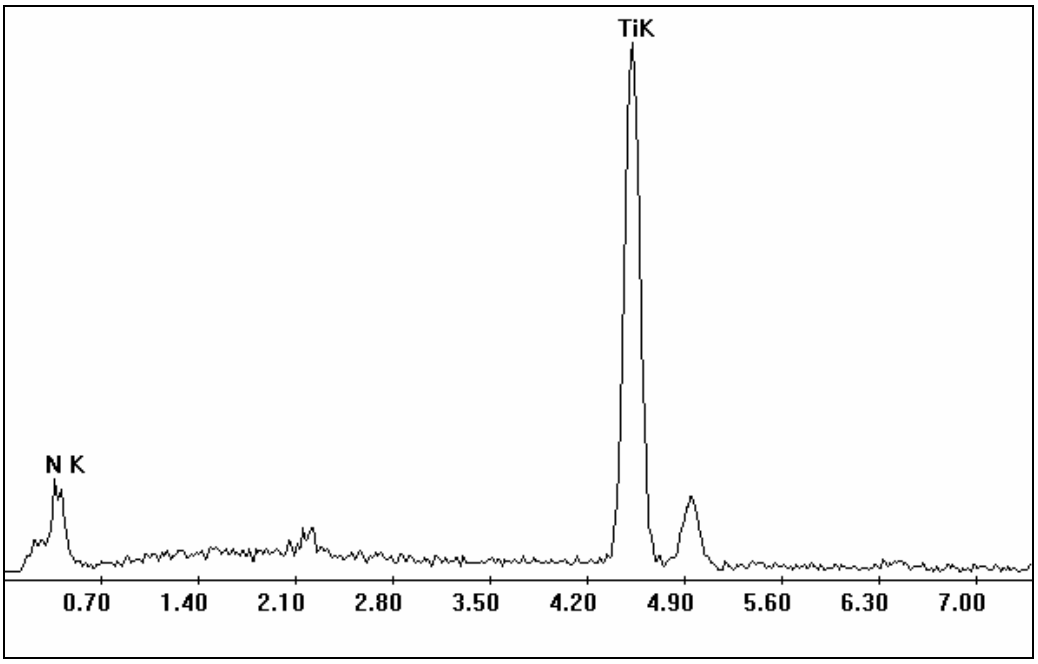

Figure 36 EDS analysis of the center of the TiN, avoiding as much of the epitaxial precipitate as possible

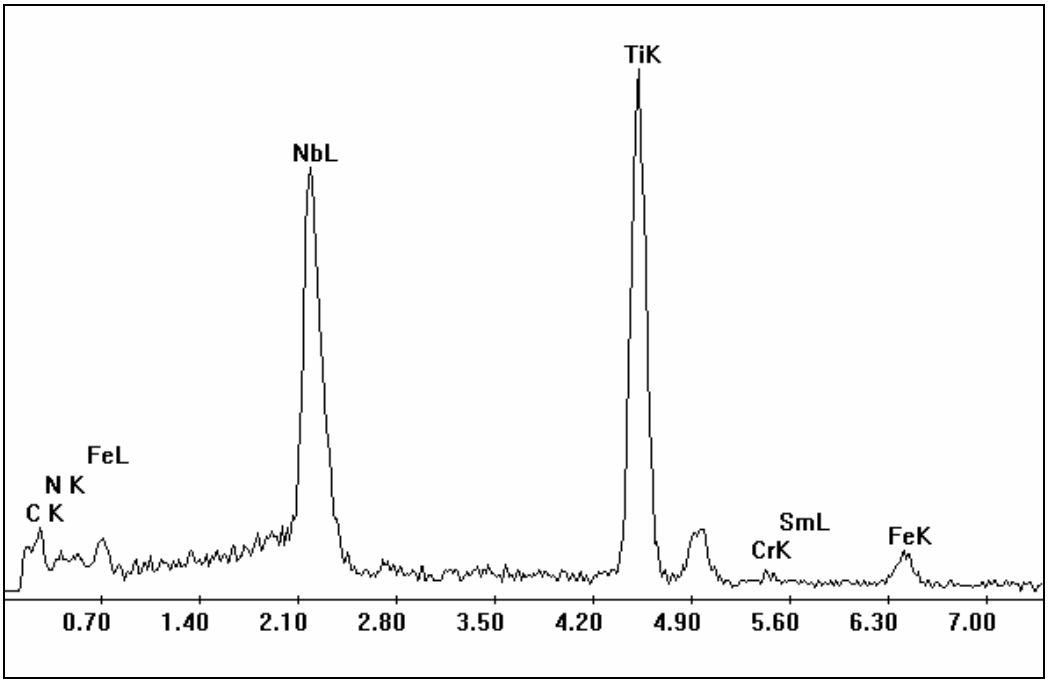

Figure 37 EDS analysis of the epitaxial (Ti,Nb)C

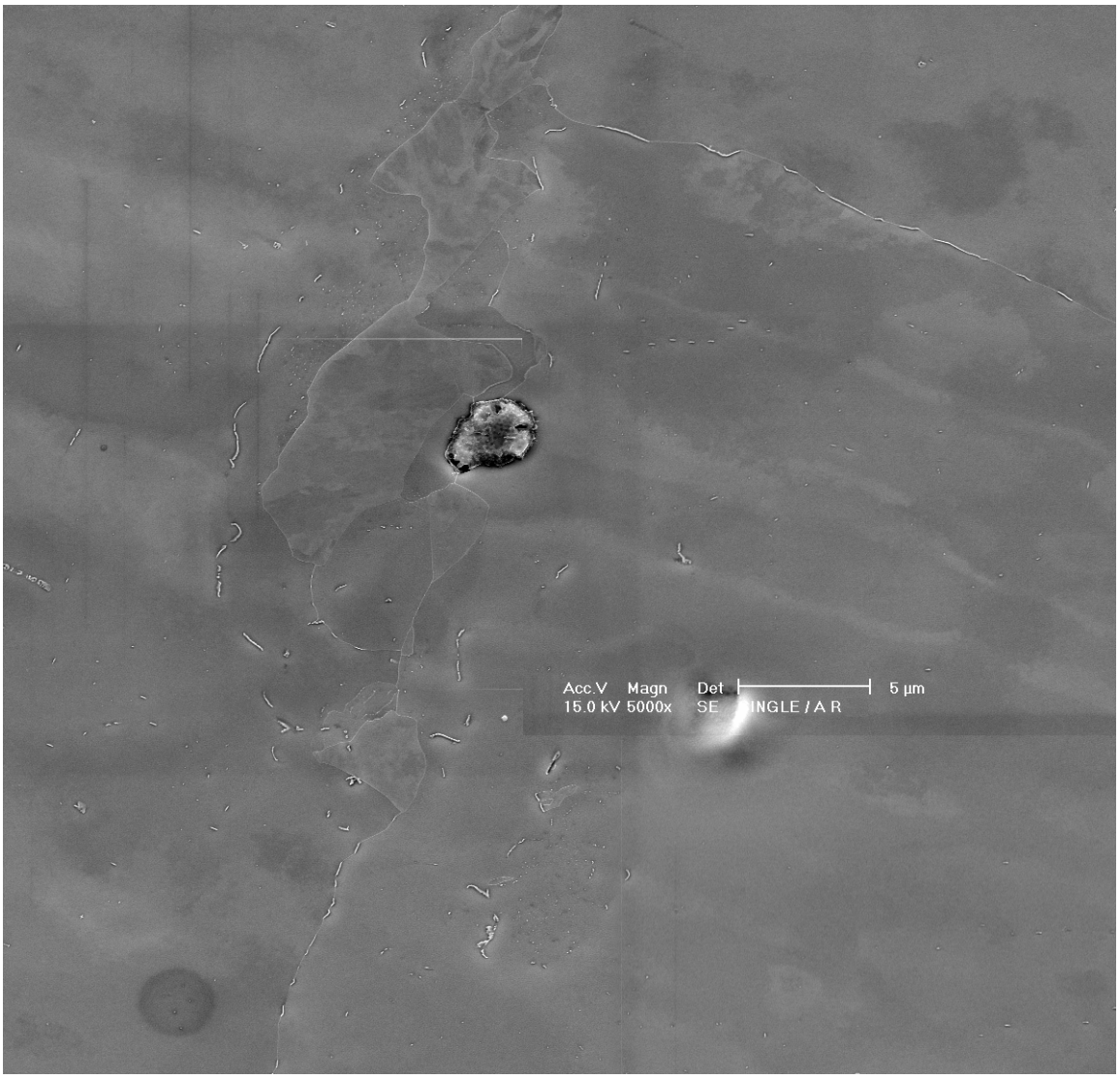

Figure 38 SEM Image of as-received Ti-Only T409

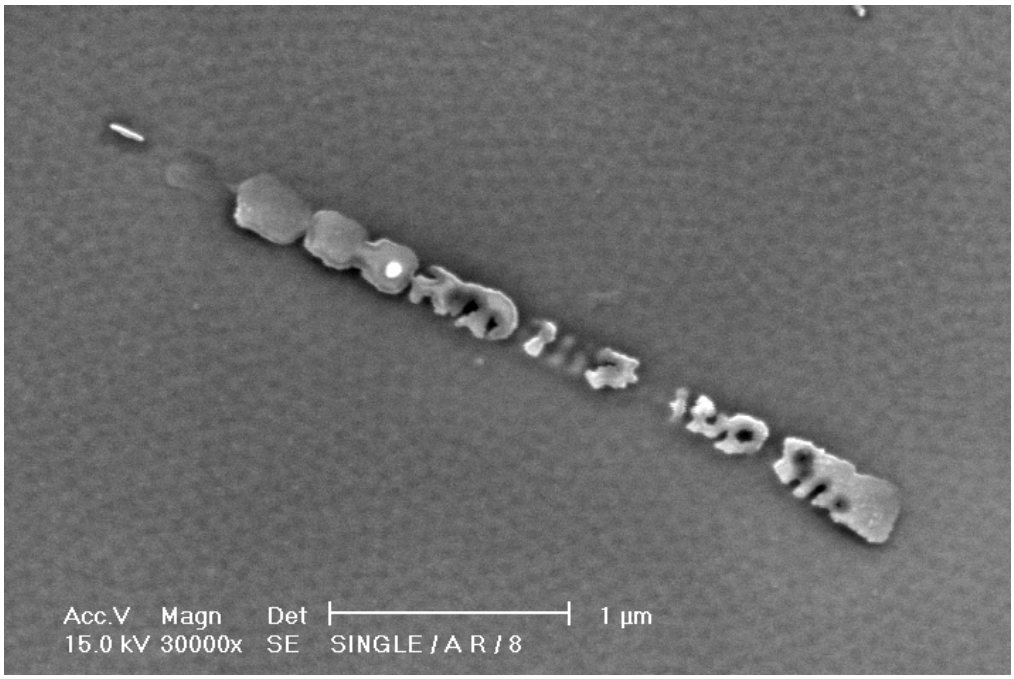

Figure 39 Eutectic-like TiC found in the as-received Ti-Only steel

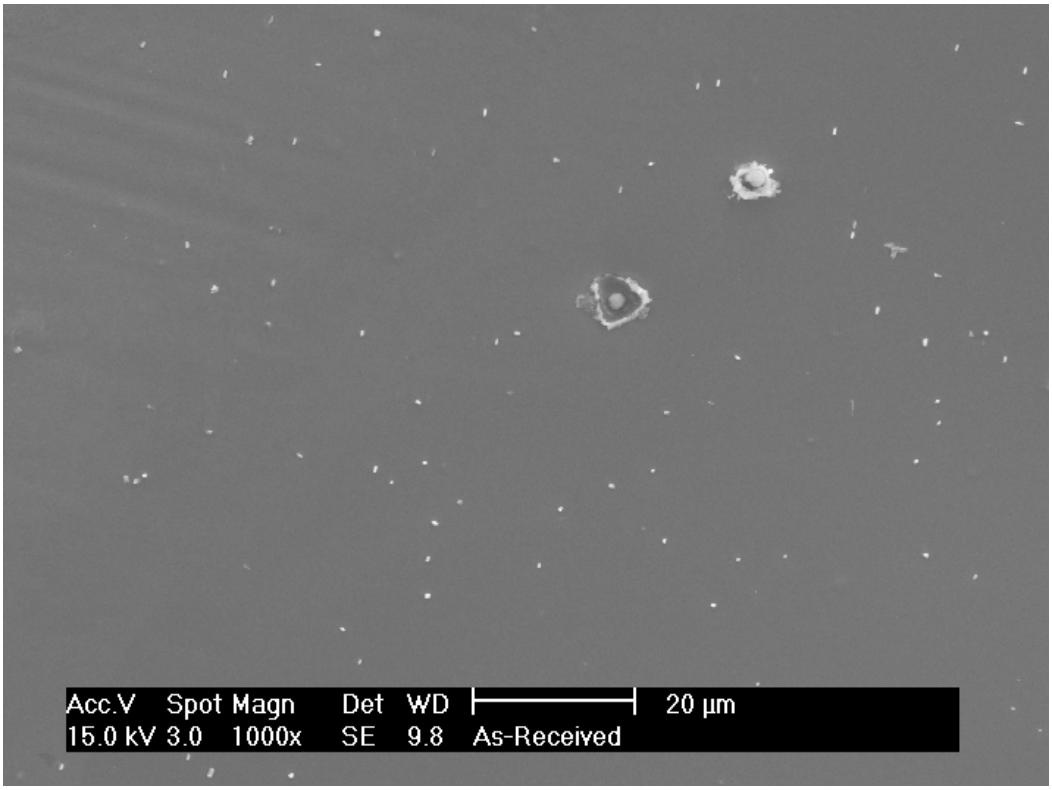

Figure 40 Matrix in the as-received dual stabilized T409, showing TiN and free-standing (Ti,Nb)C

5.2.2.2 Crystal Structure of the Precipitates

All of the precipitates found in this research showed an FCC crystal structure. The TiN could not be analyzed for crystal structure in the TEM because the particles were too large but it is generally accepted that TiN is an FCC lattice with the NaCl crystal structure[45]. The TiC and (Ti,Nb)C are also known to be of the same crystal structure. The FCC lattice in these carbides was verified using selected area diffraction on the TEM.

5.2.2.3 Orientation Relationships of Precipitates

The orientation relationship of the TiN could not be determined because they were too large for the TEM beam to penetrate. It was therefore impossible to determine the orientation of the epitaxial precipitates relative to the titanium nitrides. However, the orientation of the free standing particles with respect to the matrix was analyzed on the TEM to verify that the particles formed in ferrite. An indexed diffraction pattern for the single stabilized steel showing both the matrix and the particle spots is shown in Figure 41. From this diffraction pattern, it is clear that the free-standing particles do conform to the Baker-Nutting orientation relationship with the matrix and it can therefore be concluded that the particles were formed in ferrite and not in austenite.

5.3 Dissolution of Precipitates during Heat Treatments

The samples from Kappeler and Schaupp[39] were analyzed on the SEM and the volume fractions of free standing carbides were measured. The resulting volume fractions for the dual stabilized steel are shown in Figure 42. The volume fraction of titanium carbides in the single stabilized steel were not measured because the particles were only on grain boundaries and not distributed in the matrix. However, it was observed that the precipitates began to dissolve at

around 900 °C and were fully dissolved at 1100 °C. The volume fraction of epitaxial precipitates in either steel could not be measured due to the inhomogeneous nature of the precipitation.

It was determined through SEM work that the epitaxial precipitates in the dual stabilized steel required a heat treatment of 1300 °C for one hour to fully dissolve. SEM images of the steel after 1250 °C and 1300 °C for one hour are shown in Figures 43 and 44. In the single stabilized steel, all of the epitaxial precipitates were dissolved after 1200 °C for 1 hour, as shown in Figure 45.

5.4 Reduction of Grain Size after Reheating

After reheating for one hour at 1300 °C, the grain size grew to nearly 1mm. Since this would not accurately represent the typical microstructure through hot rolling, samples were reheated and given a 50 percent reduction at 1215 °C to reduce the grain size. The measured grain sizes before and after a 3 minute hold were as follows:

Table 9 Grain size measurements after deformation at 1215 °C

Steel Type	Conditions	Results
Dual Stabilized T409	50% ε, quench	D = 360 μm
		SD = 159 μm
	50 % ε, 3min. hold, quench	D = 436 μm
		SD = 208 μm
Single Stabilized T409	50% ε, quench	D = 415 μm
		SD = 191 μm
	50 % ε, 3min. hold, quench	D = 630 μm
		SD = 234 μm

The fact that the grain size in the dual stabilized steel was smaller both before, and to a greater extent, after the hold, indicates that there was something inhibiting the grain growth in the dual stabilized steel. Coupled with the results of the dissolution studies above and the

continuous cooling deformation results in the following section, this indicates that (Ti,Nb)C carbides in the dual stabilized steel re-precipitated during reheating and were present at 1215 °C when the deformation occurred.

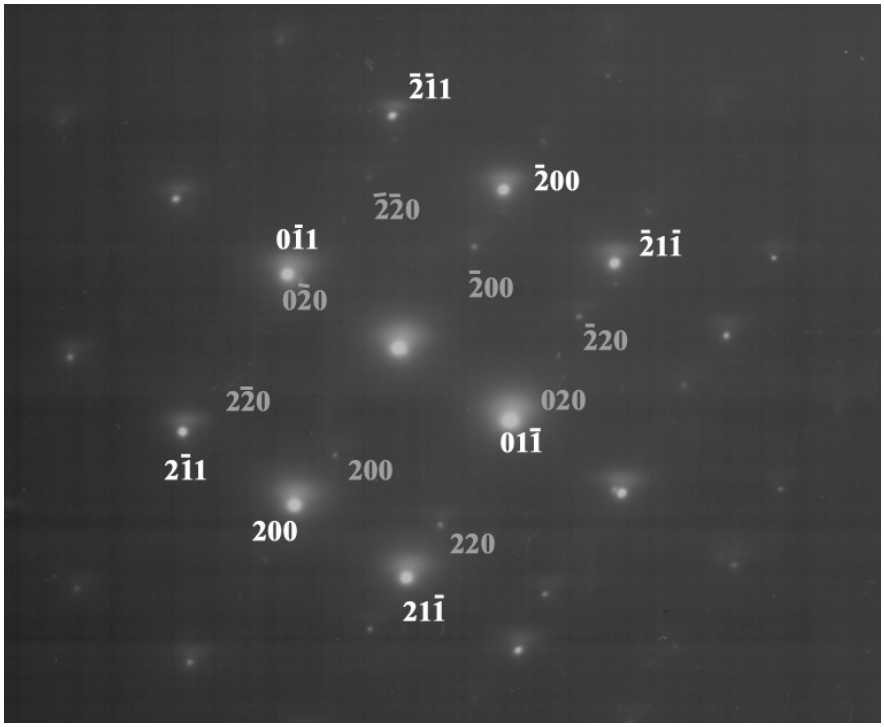

Figure 41 Indexed diffraction pattern showing the Baker-Nutting orientation relationship between a TiC particle and the matrix in the single stabilized T409. The white poles are for the matrix and the grey poles are from the particle.

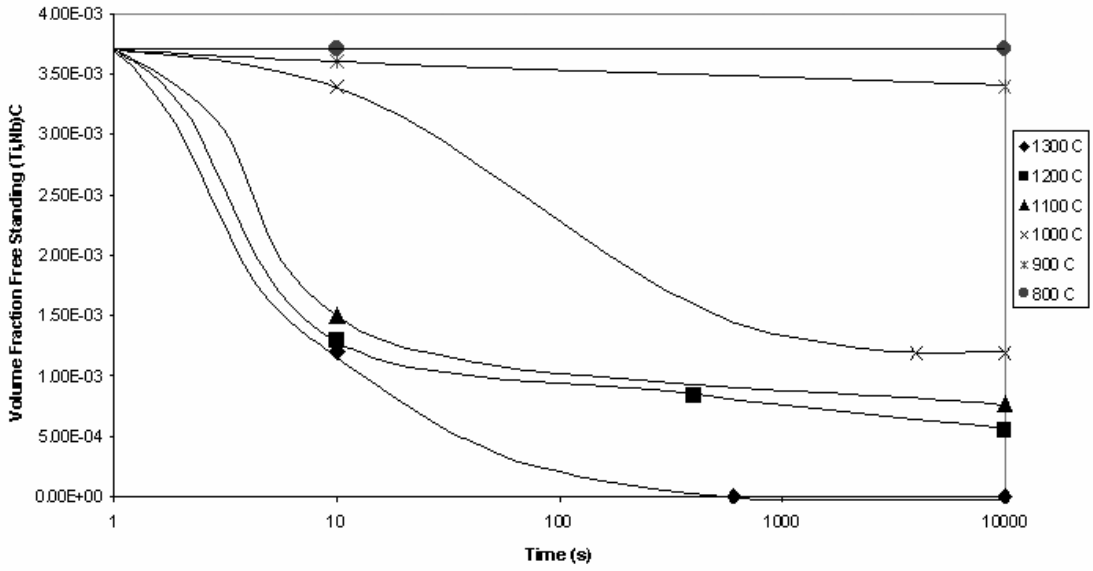

Figure 42 Measured volume fraction of free standing (Ti,Nb)C vs. time at various temperatures for the dual stabilized T409

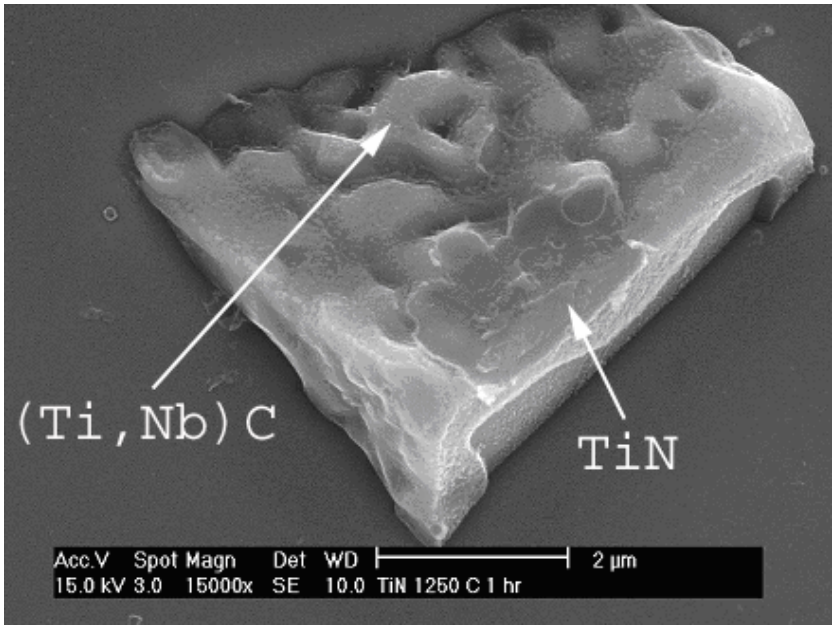

Figure 43 SEM image of a TiN particle with epitaxial (Ti,Nb)C in the dual stabilized steel after a heat treatment of 1250 °C for 60 minutes

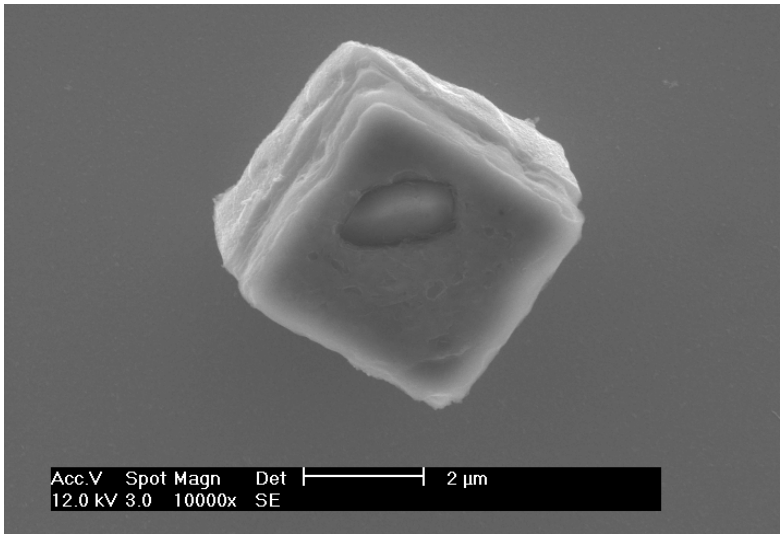

Figure 44 SEM image of a TiN particle in the dual stabilized steel after a heat treatment of 1300 °C for 1 hour

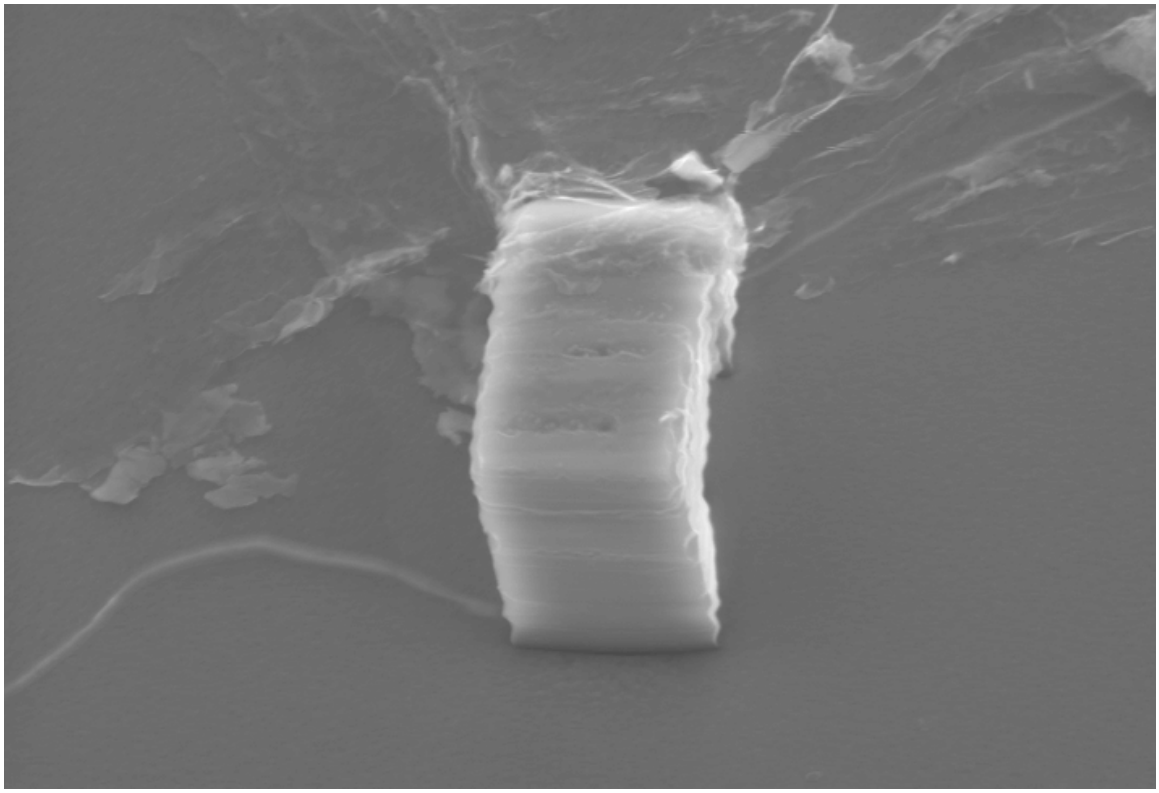

Figure 45 SEM image of a TiN particle in the single stabilized steel after a heat treatment of 1200 °C for 1 hour

5.5 Continuous Cooling Precipitation Results

5.5.1 Single Stabilized T409

Several methods were tested to determine the precipitation start temperature in the single stabilized steel (dilatometry, calorimetry, etc.) before continuous cooling deformation testing was used. However, only CCD testing proved useful in determining the precipitation start temperature for such a small amount of precipitates. A resulting flow curve from CCD testing is shown in Figure 46. Visually, it is clear that there are two inflection points in this curve. To quantify the inflections, the slope of the log[load] vs. temperature line was determined for each data point (Figure 47) and the precipitation start temperature was defined as the temperature where multiple data points exceeded the threshold deviation from linearity. The precipitation finish temperature was determined the same way except the return to linearity was measured. The resulting CCP curve for the dual stabilized steel is shown in Figure 48. To verify the start of precipitation, samples were quenched from above and below the inflection point. Above the inflection point, no titanium carbides were found. Below the inflection point, there were titanium carbides precipitated on grain boundaries and subgrain boundaries. An example of a titanium carbide particle precipitated on a subgrain boundary just below the precipitation start temperature is shown in Figure 49.

5.5.2 Dual Stabilized T409

Unfortunately, the combination of fast kinetics and high precipitation start temperature in the dual stabilized steel prevented the determination of a precipitation start temperature through CCD testing or otherexperimental procedure available in this study. The upper limit of the open-air furnace mounted on the MTS is 1225 °C. This meant that the samples had to be pre-annealed

at 1300 °C for one hour in a different furnace to dissolve the precipitates. However, when reheating in the MTS furnace, the (Ti,Nb)C re-precipitated during heating and would not dissolve at 1225 °C. Therefore, a different method, less precise method had to be used for the dual stabilized steel. To determine the start temperature for precipitation in the dual stabilized steel, samples were heated to 1300 °C in and then slow cooled and quenched from different temperatures. These samples were then analyzed on the SEM to determine the precipitation start temperatures. It was found that the dual stabilized steel precipitates both free standing and epitaxial (Ti,Nb)C at 1210°C at cooling rates from 0.1 to 10 °C per second.

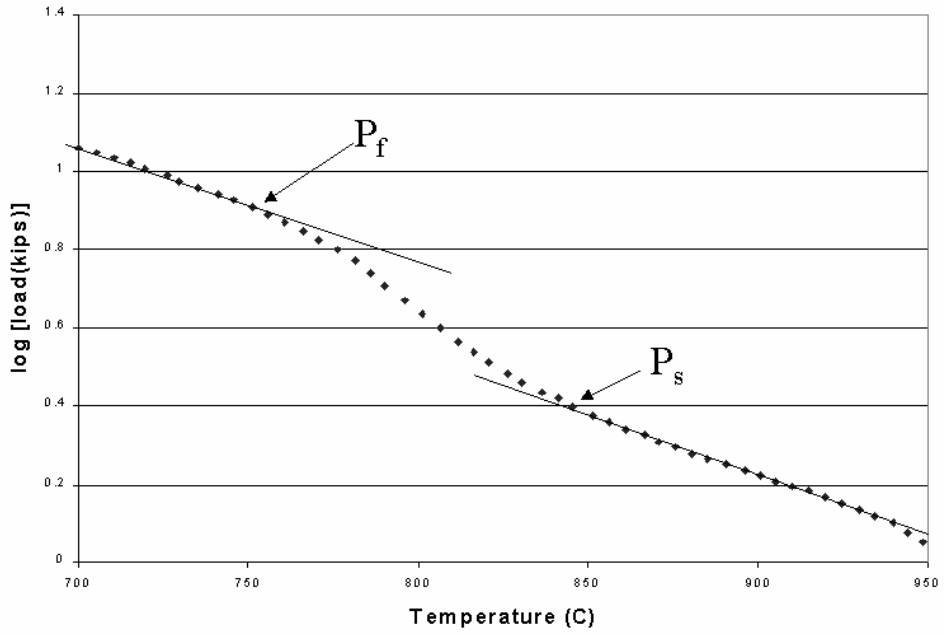

Figure 46 Flow curve for single stabilized T409 from CCD testing with a cooling rate of 2.0°C/second

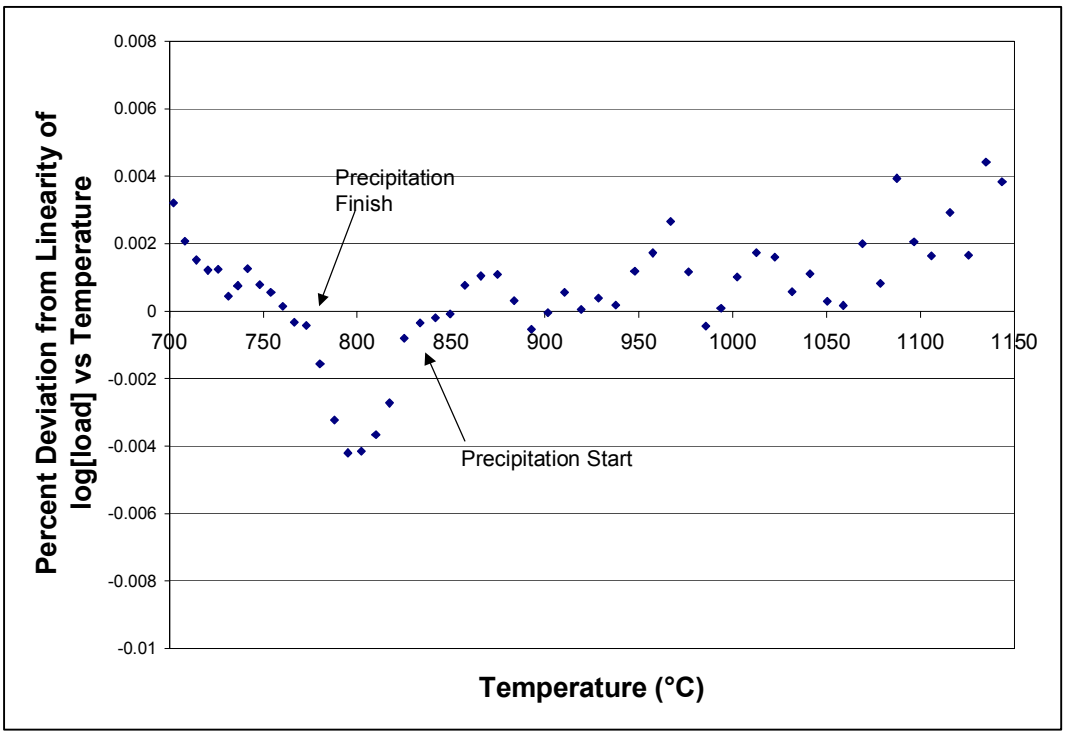

Figure 47 The slope of the log [load] vs. temperature is plotted to determine the exact precipitation start and precipitate finish temperatures

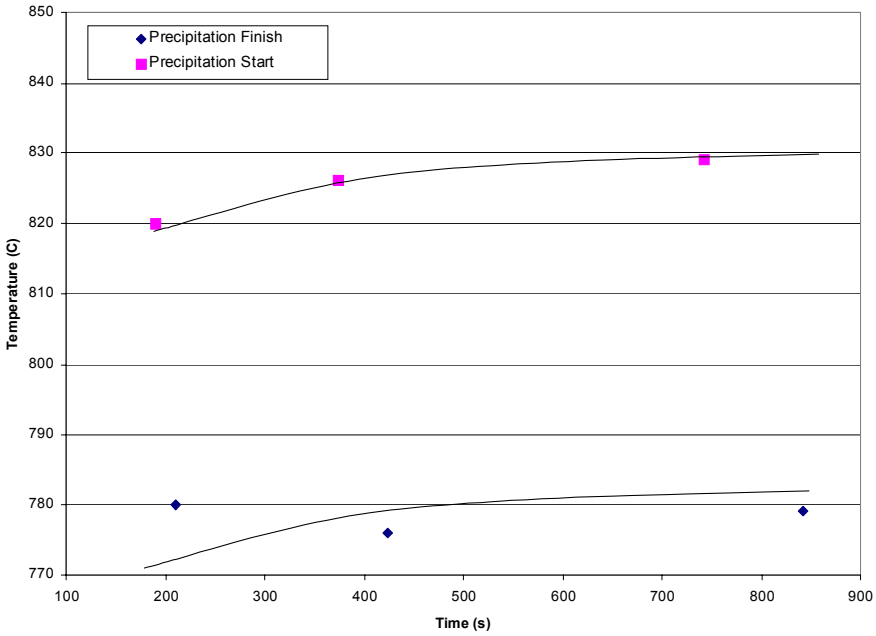

Figure 48 Continuous Cooling Precipitation (CCP) curve for single stabilized type 409

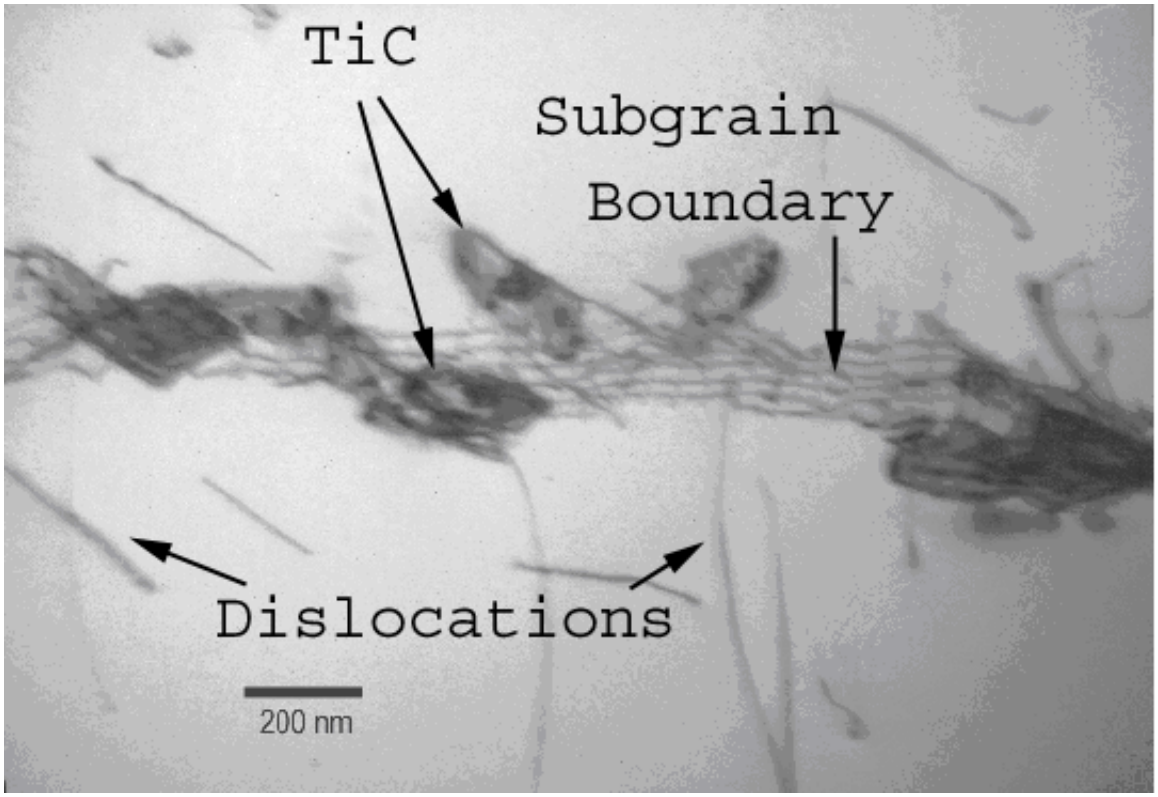

Figure 49 TEM image of titanium carbide particles precipitated on a subgrain boundary (Ti-Only T409)

5.6 Austenite Morphology/Characteristics

5.6.1 Grain Boundary Misorientation Angles – EBSD

To characterize the ferrite grain boundaries where austenite first forms, electron backscatter diffraction patterns (EBSD) were used. There were several observations that can be made from the EBSD results. First, it is clear that the austenite forms preferentially on high angle ferrite grain boundaries (>15°) as shown in Figure 50. It is also apparent that the grain boundaries where austenite forms have a bimodal distribution around 20-25º and 45-50º, indicating that the misorientation of the ferrite/ferrite grains has an influence on the nucleation of the austenite. It should also be noted that the martensite grains consistently index as ferrite, indicating a low degree of tetragonality and thus low carbon content. The measured angles between the martensite (quenched austenite) grains and the surrounding ferrite grains showed a high propensity for angles of 54 and 35 degrees with at least one of the neighboring grains (Figure 51). These angles are the two angles formed in the right triangle between a (110) and (111) plane. This shows that the austenite forms with the Kurdjumov-Sachs orientation relationship with at least one of the neighboring grains.

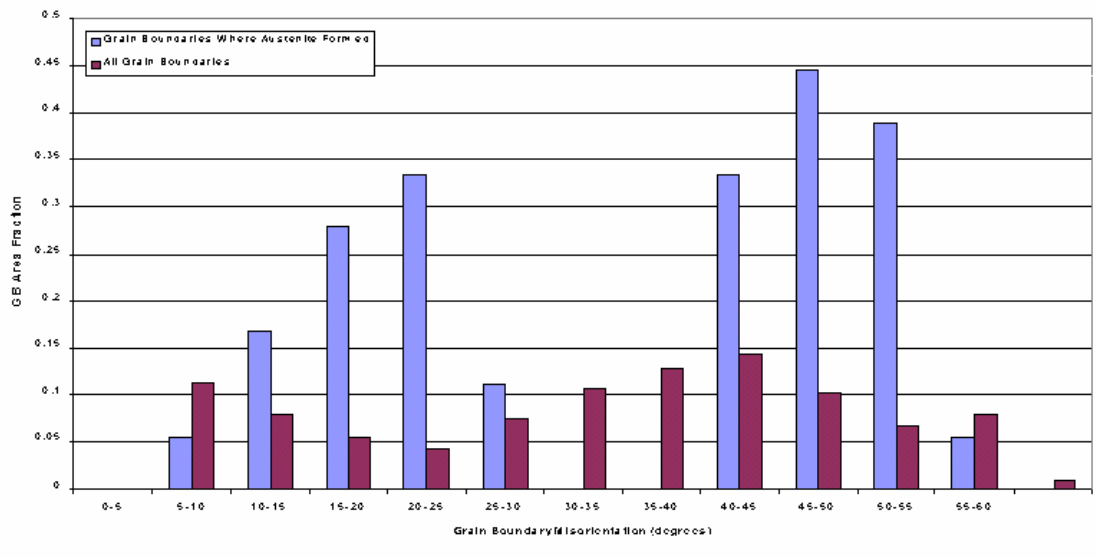

Figure 50 Grain boundaries where austenite forms compared to all grain boundaries

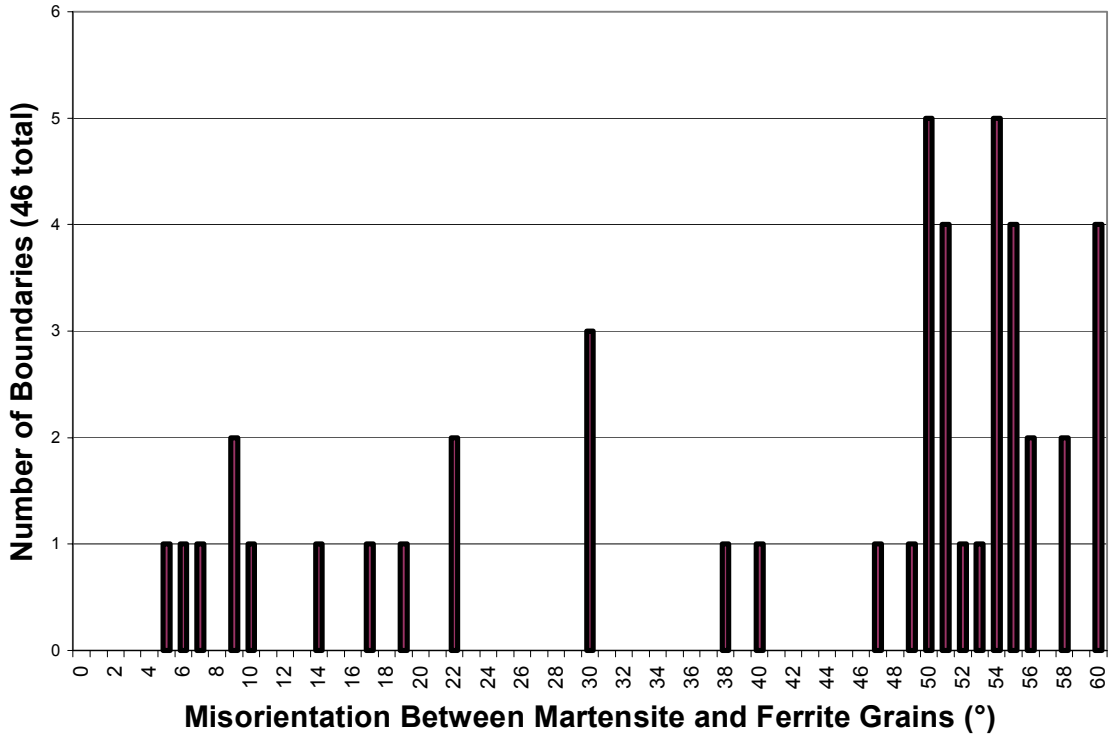

Figure 51 Misorientations between martensite and ferrite grains as measured by EBSD

6.0 DISCUSSION

6.1 Study of Precipitation

The precipitation behavior was markedly different in the two steels. The precipitation results will be discussed in the following sections. Specifically, the total amount of precipitation, the temperatures to which they are stable, and location of the precipitates, will each be discussed individually.

6.1.1 Volume Fraction of Precipitates

In the dual stabilized steel, there was a much larger volume fraction of (Ti,Nb)C precipitates in the steel. The larger volume fraction of precipitates would be expected in this study since the dual stabilized steel has higher concentrations of carbon, nitrogen, and stabilizing elements. While the single stabilized steel contains 0.0091 wt% carbon and 0.0081 wt% nitrogen, the dual stabilized steel contains 0.015 wt% carbon and 0.013 wt% nitrogen. In addition, while the single stabilized steel contains 0.22 wt% titanium, the dual stabilized steel contains 0.2 wt% titanium plus 0.15 wt% niobium. Both steels contain nearly the same ratio of (Ti+Nb)/(C+N), but there is about 1.6 times the total amount of interstitials and stabilizing elements in the dual stabilized steels. Once the volume fraction of precipitates is calculated for these steels, the result is that the dual stabilized steel will have 9.8×10^{-4} vol. percent TiN and 1.37×10^{-3} vol. percent (Ti,Nb)C. In the single stabilized steel, the result is only 6.11×10^{-4} vol. percent TiN and 7.23×10^{-4} vol. percent TiC. Therefore, the increased volume fraction of precipitates can be explained by the composition of the steels.

6.1.2 Precipitation/Dissolution Temperatures

The Ti+Nb dual stabilized T409 showed much higher dissolution and precipitation temperatures for (Ti,Nb)C than the TiC in the single stabilized steel. This can be partially explained by the higher amounts of both carbon and stabilizing elements in the dual stabilized steel. Instead of plotting the solubility product for TiC and NbC individually, a solubility product for (Ti,Nb)C was derived by using the average value of the solubility products for TiC and NbC in ferrite that were used in Section 5.1. K was taken to be ([Ti]+[Nb])[C], and the solubility product can be calculated using the composition of the dual stabilized. This new solubility product predicts precipitation at about 50 °C higher than either the TiC or NbC treated separately, as shown in Figure 52.

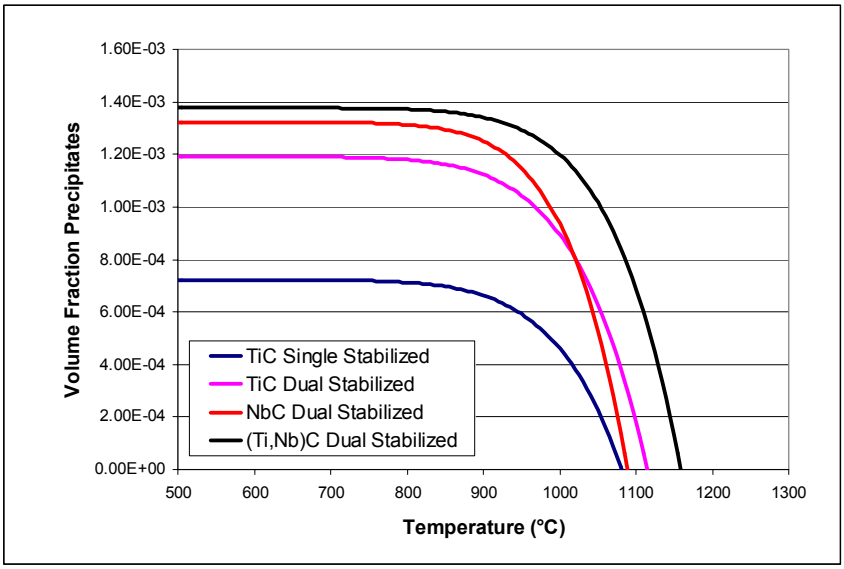

Figure 52 Predicted volume fraction of precipitates including a combined solubility product for (Ti,Nb)C

Although this does partially explain the difference in precipitation/dissolution temperatures, it also shows that there must be some sort of synergistic effect of the titanium and the niobium. It is apparent that the (Ti,Nb)C must have a higher free energy of formation in this

temperature range than either the TiC or NbC. This is evidenced by the observation that there were no TiC or NbC present in the dual stabilized steel at any temperature. Therefore, either the free energy of formation must be higher (thus a more stable particle) or there must be a diffusion or nucleation problem. Since the elements are the same, it can be assumed that diffusion cannot be the limiting factor. Also, since the lattice parameter of α-Fe (4.054) is lower than that of either TiC(4.360), NbC(4.470), or (Ti,Nb)C (varies linearly between the two), it can be concluded that the strain energy in nucleation cannot be the decisive factor. Therefore, the (Ti,Nb)C must be a more stable particle and thus have a higher free energy of formation than either the TiC or NbC individually.

6.1.3 Location of the Precipitates

In the as-received transfer bars, there was a marked difference in the location of the precipitates, as well. In the single stabilized, Ti-only steel, all of the free-standing TiC precipitates were located on the grain boundaries. However, the steel with both titanium and niobium contained free standing (Ti,Nb)C homogeneously distributed throughout the matrix. The explanation for this phenomenon derives from the higher driving force for precipitation in the dual stabilized steel. This higher driving force is obvious from the higher precipitation and dissolution temperatures. Since there is a higher driving force, the nuclei will be able to overcome more easily the free energy barrier that is caused by the surface and strain energy required to homogeneously nucleate a particle in the matrix.

Another substantial difference in the location of the precipitates was the amount of epitaxial precipitation observed on the TiN. The dual stabilized steel contained much more epitaxial precipitation than the single stabilized steel. There are several possible explanations for this phenomenon. First, the higher volume fraction of precipitates overall will lead to a higher

volume fraction of epitaxial precipitation. However, the difference in amount of epitaxial precipitates is much larger than the increase in overall precipitation observed in the dual stabilized steel. The increase in epitaxial precipitation also could possibly be explained on the basis of the lattice parameters. The lattice parameters of Ti_xNb_xC and Ti_xNb_xN are plotted in Figure 53. The lattice parameter of TiC is closer to that of TiN than NbC. Therefore, it would be expected that more precipitation would occur on the TiN in the single stabilized steel. However, since titanium, niobium, carbon, and nitrogen are all mutually soluble, it can be conceived that more complex carbonitrides could form in the dual stabilized steel. If some niobium were to diffuse into the TiN core, it would increase the lattice parameter closer to that of NbC. If, at the same time, the epitaxial particle was actually (Ti,Nb)C, then the lattice parameter of the epitaxial particle would decrease, bringing it closer to that of TiN. It could also be assumed that some of the nitrogen could diffuse into the epitaxial particle and some of the carbon could diffuse into the TiN. The final effect would be that locally, at the TiN/NbC interface, a complex (Ti,Nb)(C,N) particle could exist on both sides of the interface, resulting in a fully coherent interface.

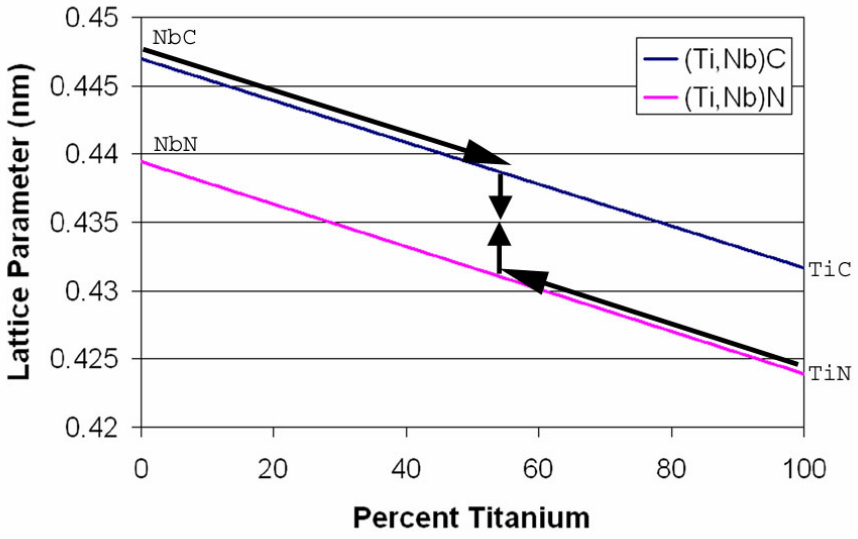

Figure 53 Schematic diagram showing the lattice parameters near the interface of the TiN and NbC in the dual stabilized steel.

6.2 Study of Austenite Formation

The formation of austenite during hot rolling is very important in ferritic stainless steels, as it can have several effects on the microstructure and properties of the final product. The formation of the austenite during hot rolling is much more complex in 11 percent chromium ferritic stainless steels than it is in low carbon or IF steels since the driving force is so much lower. In chromium steel, there are several factors that will affect the amount of austenite formed at a specific temperature and the time at which it takes for the austenite to form. These factors include the chromium content, carbon and nitrogen contents, stabilizing elements, grain size, grain boundary character and segregation of interstitials. None of these factors are considered in a low carbon steel, where an anneal at 1000 °C will still form one hundred percent austenite in a matter of seconds. Therefore, the prediction of austenite formation in type 409 ferritic stainless steel is very difficult, and more than just the composition needs to be taken into

account. To further confirm this point, Table 9 shows the composition of several T409 ferritic stainless steels that have been studied in the past and the amount of austenite observed. It is clear that the formation of austenite is not dependant on the composition alone.

One of the largest influences on the formation of austenite is the grain size. In previous research[46] on type 409, it was shown that after a 1200 °C anneal followed by isothermal holding, less than 5 percent austenite formed at any temperature due to the large grain size. In the same steel, hot band samples heated directly to 1000 °C and held for one hour had more than 50 percent austenite at a grain size of 150 μm. The same principles could be applied to the current research when considering the continuous cooling experiments. Although the grain size was reduced from the reheating grain size, it was still much larger than the typical grain size during hot rolling. This means that even though no austenite was formed during these continuous

Table 10 Compositions of several 11 percent chromium ferritic stainless steels that were investigated by different authors and the amount of austenite observed in the steels

Authors	Sample Code	Cr	C	N	Nb	Ti	Starting Condition	Observations
Raabe and Lucke (1993)	Cr11Ti	11.3	0.01	0.01	------	0.21	3mm Hot Band	Presence of austenite during HR weakens Hot band Texture
Raabe and Lucke (1993)	Cr11Nb	10.5	0.01	0.02	0.32	0.11	3mm Hot Band	Presence of austenite during HR weakens Hot band Texture
Raabe (1996)	11Cr	11	*	*	*	*	*	90 % austenite (estimated from texture results)
Raabe (1996)	15Cr	15	*	*	*	*	*	78% austenite (estimated from texture results)
Raabe (1996)	17Cr	17	*	*	*	*	*	15 % austenite (estimated from texture results)
Moses (1994)	IF Ti Stab.	11.1	0.002	0.005	<0.01	0.23	13mm Hot Band	No austenite found in continuous cooling experiments
Moses (1994)	IF Ti & Nb. Stab.	11.1	0.003	0.004	0.1	0.09	13mm Hot Band	No austenite found in continuous cooling experiments
Clint Graham (1998)	T409	10.95	0.01	0.02	0.00	0.20	25.4cm Hot Band	(isothermal) 69% at 1200 °C, 2 hr, 76 percent at 1065 °C, 30 min
Clint Graham (1998)	T466	11.06	0.03	0.01	0.16	0.19	25.4cm Hot Band	(isothermal) 44% at 1200 °C, 2 hr, 66 percent at 1065 °C, 30 min
Nooning, Denardo (1999)	T409 (Ti)	11.01	0.013	0.019	0.006	0.17	5mm Hot band	(isothermal) max 25% at 1025 °C, range from 900-1150 °C
Nooning, Denardo (1999)	T409 (Ti+Nb)	10.98	0.019	0.01	0.15	0.18	5mm Hot Band	(isothermal) max 52% at 1025 °C, range from 900-1150 °C
Kappeler, Schaupp (2000)	T409 (Ti)	11.0	0.0091	0.0081	0.007	0.22	25.4 cm Tranfer Bar	(isothermal) max 33% at 1100 °C, range from 900 to 1200 °C
Kappeler, Schaupp (2000)	T409 (Ti+Nb)	11.07	0.015	0.013	0.15	0.20	25.4 cm Tranfer Bar	(isothermal) max 41% at 1100 °C, range from 900 to 1200 °C

cooling experiments, the possibility of austenite during hot rolling cannot be ruled out since a smaller grain size and large amounts of deformation were not investigated in this work. It is clear from the above Table that other steels of similar compositions did form austenite, and, therefore, it could still be possible in this steel.

Another influence on possible austenite formation would be the choice and amount of stabilizing elements. Traditionally, austenite needs carbon to form in ultra low carbon steels. By applying this same idea to ferritic stainless steels, it would seem that the austenite would need carbon to form. Therefore, if enough stabilizing elements were added so that all of the carbon would be tied up in precipitates at a high enough temperature, there would be no carbon available for the formation of austenite and thus the transformation would be suppressed. However, it is not yet clear how much of an effect the carbon content has on the formation of austenite in these steels. Furthermore, it is not clear whether a reduction in the solute carbon will affect the equilibrium amount of austenite of if it will simply slow down the kinetics of the reaction.

The grain boundary structure and character could also have an effect on the austenite formation. It has been shown that the austenite forms with a low energy boundary with one ferrite grain and with a high energy boundary with the other ferrite grain. It has also been observed that austenite does not form on all grain boundaries simultaneously. Therefore, some condition exists at select grain boundaries that make them the first nucleation sites for austenite. This could be either a segregation of elements to select grain boundaries or a special grain boundary misorientation. Since we know that the austenite does form with a special grain boundary on at least one side, it can be theorized that a proper misorientati on between ferrite grains could decrease the free energy necessary for nucleation and growth of austenite and

increase the probability of austenite forming at that grain boundary. Therefore, steels with a higher proportion of these special boundaries could form more austenite in a shorter amount of time.

6.3 Effect of Results on Microstructure and Mechanical Properties

6.3.1 Effects of Higher Dissolution/Precipitation Temperature in the Dual Stabilized Steel

The higher dissolution/precipitation temperature in the dual stabilized steel will have many effects on the final microstructure and properties of the steel. These effects are derived from the difference in the location of the solutes in the temperature range of 850-1150 °C. In the dual stabilized steel, all of the carbon will be tied up in (Ti,Nb)C precipitates. A large portion of the titanium and niobium will also be tied up in these precipitates. By contrast, all of the carbon will still be in solution at these temperatures in the single stabilized steel. This will have many effects during both hot rolling and cold rolling and annealing.

6.3.1.1 Effects of Carbon in Solution

The largest effects of the carbon in solution will be evident during hot rolling. If the roughing passes begin below 1150 °C, all of the carbon will be tied up in (Ti,Nb)C before the rolling begins in the dual stabilized steel. By contrast, the carbon will remain in solution up until coiling in the single stabilized steel. The carbon content in solution for both steels during typical hot rolling can be shown schematically as in Figure 54. This difference in carbon content could have direct effects on the microstructure in terms of the amount of austenite formed and the hot band texture. Since the carbon in solution can directly affect the amount of austenite formed during hot rolling, it could be theorized that the dual stabilized steel will form less austenite during hot rolling, as shown in Figure 55. This austenite will have significant effects on the final

properties of the steel. Research has shown[47,48] that the formation of austenite during hot rolling can significantly weaken the hot band texture. Therefore, the dual stabilized steel will be expected to have a stronger texture in the hot band, which would remain even after cold rolling and annealing. As shown in Section 2.2.1, the carbon will also have direct effects on the hot band texture. The lower carbon content in solution in the dual stabilized steel can increase the strength of the {111} texture and in turn increase the formability (figure 2). In addition to affecting the texture, the austenite in the steel during hot rolling could also transform to martensite if the steel is water cooled before coiling. This martensite in the hot band would cause defects during cold rolling due to the fact that the martensite would be much harder than the surrounding ferrite matrix.

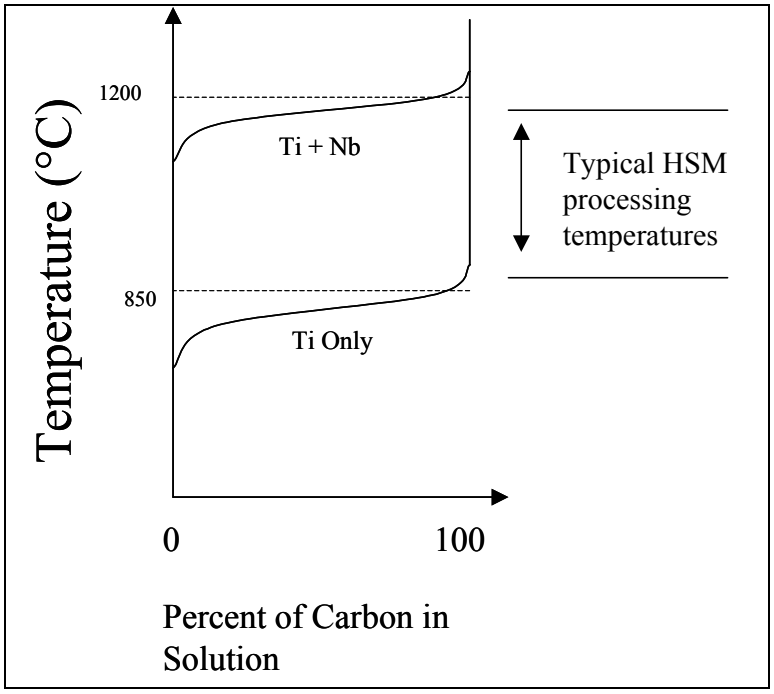

Figure 54 Schematic showing the difference in solute carbon during hot rolling between the two steels

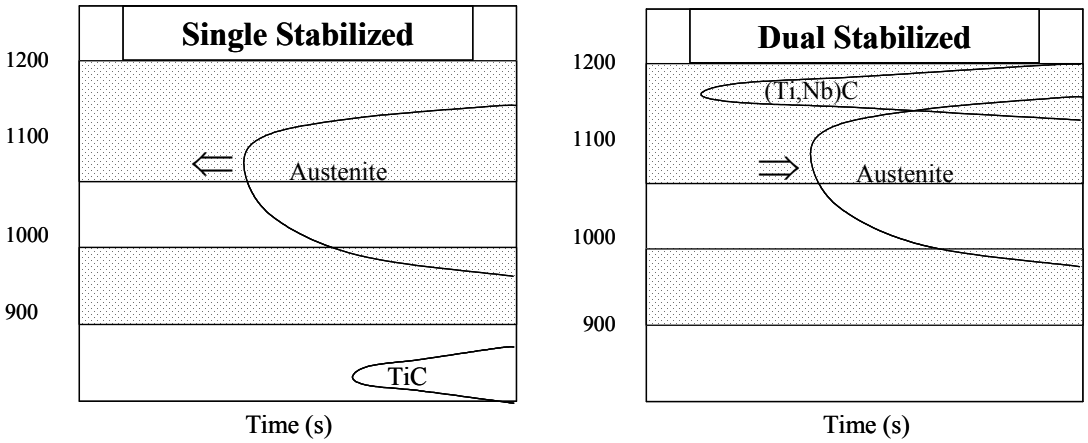

Figure 55 Effect of precipitation on carbon content and austenite formation during hot rolling

6.3.1.2 Effects of Precipitates

In addition to the solute carbon, the fact that the carbides in the dual stabilized steel form at and are stable to higher temperatures will also have effects on the microstructure and mechanical properties. Except for when these precipitates first form, which is usually above the first pass of hot rolling, the precipitates are too large to inhibit recrystallization. However, the volume fraction and size of the precipitates can be effective at pinning grain boundaries, as shown by the grain size studies in Section 5.4. Other work (Rege[17], Kappeler and Schaupp[40]) has also shown that the carbides can be effective at pinning grain boundaries. This means that the dual stabilized steel should show a smaller final grain size due to the suppression of grain growth by the particles. However, not only will these precipitates block the movement of grain boundaries, but they will only stop the movement of some grain boundaries. It has been shown by Raabe and Lucke[47,48] that the particles in the dual stabilized T409 ferritic stainless steel will block only high energy grain boundaries in a process known as selective particle drag. This leads to a difference in the final texture after cold rolling and annealing between the single stabilized and dual stabilized steels. The size of the carbide precipitates has also been shown to affect the final texture by particle enhanced nucleation[17].

7.0 CONCLUSIONS

1. Dual Stabilized T409 ferritic stainless steel shows a marked difference in precipitation behavior compared to the single stabilized steel:
    a. Greater amount of epitaxial carbide precipitation on pre-existing TiN
    b. Larger fraction of free-standing carbides in the matrix as opposed to on grain boundaries
    c. Higher dissolution/precipitation temperature of the carbides
2. The formation of austenite in these steels is strongly dependent on several factors:
    a. Grain size
    b. Solute carbon content
    c. Choice of stabilizing elements
    d. Grain boundary misorientations between ferrite grains
3. The observed differences in final properties of these steels are due to the differences in precipitation behavior between the two stabilizing systems. The higher precipitation/dissolution temperature can lead to:
    a. Large differences in the final texture due to the precipitates in the dual stabilized steel that will be present during hot rolling and during annealing
    b. Large variations in the final texture due to the increased solute carbon content of the single stabilized steel during hot rolling and annealing
    c. Martensite in the hot band of the single stabilized steel due to a higher solute carbon content
    d. Possible differences in grain size due to pinning of grain boundaries by the precipitates in the dual stabilized steel

BIBLIOGRAPHY

BIBLIOGRAPHY

1. Blickwede, D.J., "Strain hardening and Anisotropy," Metal Progress, January 1969, pp. 84-87.

2. Lankford, W.T. et al., "New Criteria for Predicting the Press Performance of Deep Drawing Sheets," Transactions of the ASM, Vol. 42, 1950, p.1197.

3. Hutchinson, R.L., Metallurgy of Vacuum Degassed Products, TMS-AIME, ed. R. Pradham, Warrendale, PA, 1990, pp. 109-125.

4. Graville, B.A., "Cold Cracking in Welds in HSLA Steels," Welding of HSLA (Microalloyed) Structural Steels, Conference Proceedings, 9-12 November, 1976, Rome, Italy.

5. Ujiro, T., Kitazawa, M., and Togashi, F., "Corrosion of Muffler Materials in Automotive Exhaust Gas Condensates," MP, Dec. 1994, pp.49-53.

6. Douthett, Joseph A., "Designing Stainless Exhaust Systems," Automotive Engineering, Nov. 1995, 45-49.

7. Beddoes, Jonathon, and Parr, J. Gordon, Introduction to Stainless Steels, 3rd ed., ASM International, Materials Park, Ohio, 1999.

8. Smith, William F., Structure and Properties of Engineering Alloys, 2nd ed., New York: McGraw-Hill Publishing Co., 1993.

9. Verhoeven, J.D., Fundamentals of Physical Metallurgy, John Wiley & Sons, New York, 1975, p. 220.

10. "Stainless Steel, Allegheny Ludlum MF-1 (Type 409)," Allegheny Ludlum Steel Corporation Blue Sheet, Pittsburgh, PA, 1974.

11. Cihal, V. Intergranular Corrosion of Steels and Alloys. New York: Elsevier Science Publishing Company, 1984. p. 205.

12. DeArdo, A.J., Garcia, C.I., Hua, M., and Tither, G., "Dual Stabilized Ferritic Stainless Steels For Demanding Applications Such As Automotive Exhaust Systems," Iron and Steelmaker, April 1997, pp. 41-44.

13. Hill, J.B., "Ferritic Stainless Steel," U.S. Patent 4,964,926, October 23, 1990.

14. Fritz, James D., and Franson, Ivan A., "Sensitization and Stabilization of Type 409 Ferritic Stainless Steel," Materials Selection and Design: MP, August 1997, 57-61.

15. Jones, D.A., Principles and Prevention of Corrosion, Simon & Schuster, New Jersey, 1996.

16. "Preliminary Data Bulletin: Stainless Steel AL 466," Allegheny Ludlum Steel Corporation, Pittsburgh, PA, 1988.

17. Rege, J., "Annealing Behavior and Formability of Low Intersticial Ferritic Stainless Steels," M.S. Thesis, Materials Science and Engineering, University of Pittsburgh, 1993.

18. Y. Xu et al., "Annealing Behavior and Formability of Ferritic Stainless Steels," Proc. Int. Symp. On Low Carbon Steels for the 90's, eds. R. Asfahani and G. Tither, TMS, Warrendale, PA, 1993, pp. 397-404.

19. Webster, D., and Woodhead, J.H., "Effect of 0.3% Niobium on the Ferrite Grain Size of Mild Steel," J. Iron Steel Inst., 202 (1964), 987-994.

20. Le Bon, A., Rofes-Vernis, J., and Rossard, C., Recrystallization and Precipitation During Hot Working of a Nb-Bearing HSLA Steel," Metal Science, 13 (1979), 238-245.

21. Fujita, N., Ohmura, K., Kikuchi, M., Suzuki, T., Funaki, S., and Hiroshige, I., "Effect of Niobium on High-Temperature Properties for Ferritic stainless steel", Scripta Materialia, Vol 35, No. 6 (1996), pp. 705-710.

22. Ruiz-Aparicio, Luis J., Garcia, C.I., and DeArdo, A.J., "Development of {111} Texture in Intersticial Free Steels," Metall. Trans. A, 32A (2) (2001), 417-423.

23. Dillon, C.P., Corrosion Resistance of Stainless Steels, Marcel Dekker, Inc., New York, 1995.

24. Xu, Y. et al., "Annealing Behavior and Formability of Ferritic Stainless Steels," Low Carbon Steels for the Nineties, (Warrendale, PA: TMS-AIME, 1993), 397-404.

25. Palmiere, Eric J., "Suppresion of Recrystallization during the Hot Deformation of Microalloyed Austenite," PhD thesis, University of Pittsburgh, 1991.

26. DeArdo, A.J., "Fundamental Metallurgy of Niobium in Steel," Niobium 2001, AIME-TMS, 2001.

27. Gladman, T., The Physical Metallurgy of Microalloyed Steels, Institute of Materials, London, England, 1997.

28. Palmiere, E.J., "Precipitation Phenomena in Microalloyed Steels," Microalloying '95, Pittsburgh, PA, June 11-14, 1995, ISS, Warrendale, PA, 1995.

29. Porter, D.A., and Easterling, K.E., Phase Transformations in Metals and Alloys, 2nd ed., New York: Chapman & Hall, 1992, p. 266.

30. Craven, A.J., He, K., Garvie, L.A.J., and Baker, T.N., "Complex Heterogeneous Precipitatin in Titanium-Niobium Microalloyed Al-Killed HSLA Steels – I. (Ti,Nb)(C,N) Particles," Acta Mat. Vol 48 (2000), pp. 3857-3868.

31. Craven, A.J., He, K., Garvie, L.A.J., and Baker, T.N., "Complex Heterogeneous Precipitation in Titanium-Niobium Microalloyed Al-Killed HSLA Steels – II. Non-Titanium based Particles," Acta Mat. Vol 48 (2000), pp. 3869-3878.

32. Sheppard, T., and Richards, P., "Structural and Substructural Observations during Thermomechanical Processing of Two Ferritic Stainless Steels," J. of Mat. Sci., Vol. 22, 1987, pp. 1642-1650.

33. Freundlich, H., Kapillarchemie, Akdd, Verlagsges, Liepzig, 1922.

34. Gladman, T., The Physical Metallurgy of Microalloyed Steels, Institute of Materials, London, England, 1997, p.48.

35. Ashby, M.F., Oxide Dispersion Strengthening, AIME, New York, 1966, p.61.

36. Gladman, T., Dulieu, D., and McIvor, I.D., Microalloying 75, Union Carbide Corporation, New York, 1976, p. 32.

37. Orowan, E., Dislocations and Mechanical Properties, Dislocation s in Metals, (ed. By M. Cohen), AIME, New York, New York, 1954.

38. Leslie, The Physical Metallurgy of Steels, McGraw Hill, New York, 1981, p. 198.

39. Brown, L.M., and Ham, R.K., "Dislocation-Particle Interactions," Strengthening Methods in Crystals, ed. By A. Kelly and R.B. Nicholson, Applied Science Publishers Ltd, London, England, 1971.

40. Kappeler, R.L., and Schaupp, M.D., "Physical Metallurgy of Ferritic Stainless Steel," Senior Thesis, Department of Materials Science and Engineering, University of Pittsburgh, 2000.

41. Hanzaki, A. Zarei, Pandi, R., Hodgson, P.D., and Yue, S., "Continuous Cooling Deformation Testing of Steels," Metallurgical Transactions A, vol. 24A, December 1993, pp. 2657-2665.

42. Moses, R., Hanzaki, A. Zarei, Yue, S., and Jonas, J.J., "Precipitation Behavior of IF 409 Ferritic Stainless Steel," 35th MWSP Conf. Proc., ISS-AIME, Vol. XXXI, 1994, pp. 435 – 442.

43. Sikaly, W., Soto, R., Bano, X., Issartel, C., Rigaut, G., and Charai, A., "Advanced Microscopy Techniques Resolving Complex Precipitates in Steels," The European Journal of Physics, AP 6 (1999), 243-250.

44. Hua, M.J., "Precipitation Behavior in Intersticial-Free Steels Containing Titanium and Niobium", PhD Thesis, Department of Materials Science and Engineering, University of Pittsburgh, 1994.

45. Pearson, W.B., Pearson's Handbook of Crystallographic Data for Intermetallic Phases. Metals Park, Oh : American Society for Metals, 1985.

46. Nooning, R.G., and Denardo, T., "Precipitation and Stabilization of T409 Ferritic Stainless Steels," Senior Thesis, Department of Materials Science and Engineering, University of Pittsburgh, 1999.

47. Raabe, D., and Lucke, K., "Textures of ferritic stainless steels," Materials Science and Engineering, Vol 9 (1993), pp. 302-312.

48. Raabe, D., "On the influence of the chromium content on the evolution of rolling textures in ferritic stainless steels," Journal of Materials Science, Vol. 31 (1996), pp. 3839-3845.